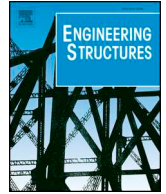




ELSEVIER

Contents lists available at ScienceDirect

Engineering Structures

journal homepage: www.elsevier.com/locate/engstruct

Seismic behaviour of innovative composite walls with high-strength manufactured sand concrete

Minsheng Guan^a, Wenting Liu^a, Mianheng Lai^{b,*}, Hongbiao Du^a, Jie Cui^b, Yangyu Gan^a

^a College of Civil Engineering, Shenzhen University, Shenzhen 518060, China

^b School of Civil Engineering, Guangzhou University, Guangzhou 510006, China

ARTICLE INFO

Keywords:

Composite wall
Concrete-filled-steel-tube
High-strength manufactured sand concrete
Ring stirrup
Seismic behaviour

ABSTRACT

Reinforced concrete (RC) walls have been widely used in tall building construction to resist lateral loads. However, RC walls behave low ductility and limited deformation capacity under high axial force ratio. Due to the brittle behaviour of high-strength concrete, it was seldom used in RC walls though it has a vast of merits compared with normal-strength concrete. To further push up the limit of concrete strength, i.e., beyond 80 MPa in practical wall construction and to figure out a possible alternative of river sand due to the sustainability and environmental friendly requirement, an innovative wall, namely ring-stirrup concrete-filled-steel-tube (CFST) composite wall with high-strength manufactured sand concrete is proposed. The proposed composite wall consists of two CFST columns embedded at each boundary element and several stirrups in the form of continuous ring along the entire section. A series of quasi-static tests based on orthogonal experimental design method (Taguchi method) are conducted to investigate the seismic behaviour of the composite walls. The experimental parameters are axial force ratio, steel ratio in CFST columns and volume ring-stirrup ratio. From the experimental tests, it is concluded that the proposed confining schemes are highly effective in improving the seismic behaviour of the walls. Moreover, the effects of these three parameters on the peak strength, ductility and energy dissipation capacity of the walls have been investigated. Finally, a design approach considering the confinement effect of CFST columns is proposed and verified to evaluate the lateral load-carrying capacity of the proposed walls.

1. Introduction

Traditionally, reinforced concrete (RC) walls have been adopted in tall building construction thanks to their high lateral stiffness and strength. Research studies [1–4] have revealed that RC walls behave low ductility and limited deformation capacity under high axial force ratio, which is defined as compressive axial force acting on the wall to the load-carrying capacity (concrete compressive strength multiply the gross section area of wall) ratio when subjected to lateral cyclic loads. Mainly two types of approaches have been adopted to solve these problems formerly. The first one is to limit the axial force ratio, which is commonly adopted in current seismic design code [5–7]. As an example, Chinese Code for seismic design of buildings [7] suggests that the design axial force ratio should be smaller than 0.5 for tall buildings in severe seismic zones. One of the consequences by adopting this method is the increase in the size of the wall, especially in the lower floor of tall buildings, which occupies the usable floor area and is undesirable for engineers and architects. The second one is to change the

configuration and reinforcement details of the wall, especially in the wall boundary, as suggested by design codes [5–7]. This can be achieved by providing transverse reinforcement (or stirrup) at close spacing to confine the concrete core in this special area. However, due to the arching action [8], the concrete core cannot be fully confined. Nowadays, high-strength concrete (HSC) is easily achievable, which can offer a better solution than normal-strength concrete (NSC) in RC walls of tall buildings since it can: (1) decrease the member size by increasing the strength-to-weight ratio and stiffness of the structures; (2) reduce the embodied carbon of construction and enhance urban sustainability; (3) maximize usable floor space, etc. But up to now, the application of such concrete in RC walls is very rare owing to its brittleness. Though by installing stirrups can provide confining stress to improve its ductility, the effectiveness of which decreases as the concrete strength increases [9–14]. Therefore, when concrete strength ≥ 80 MPa, to restore reasonable level of ductility that can be used in practical wall construction, the content of stirrup required will be too large to ensure acceptable concrete placing quality. Thus, the use of HSC in

* Corresponding author.

E-mail address: laimianheng@gzhu.edu.cn (M. Lai).

<https://doi.org/10.1016/j.engstruct.2019.05.096>

Received 29 January 2019; Received in revised form 29 April 2019; Accepted 28 May 2019

0141-0296/ © 2019 Elsevier Ltd. All rights reserved.

conventional type of RC walls is not appropriate.

To further push up the limit of concrete strength, i.e., beyond 80 MPa in practical walls construction and to improve the seismic behaviour of walls, recently, many research studies have been conducted on the composite walls, which combine the advantages of the construction materials, i.e. concrete, steel plate, steel tube and FRP [15–20]. The provision of steel tube [21,22] or FRP, forming concrete-filled-steel-tube or FRP-confined concrete wall allows a more uniform, continuous and larger confining stress but not jeopardize the wall concrete pouring quality [23–27]. Thanks to the composite action between the steel/FRP and concrete, when acting as the boundary elements, the composite walls behave in a ductile manner with large lateral load-carrying and deformation as well as fat energy dissipation capacities even subjected to high axial force ratio (> 0.5) under cyclic lateral load. For example, Qian et al. [15] proposed the steel tube-reinforced concrete composite wall, with different configuration of concrete-filled-steel-tube (CFST) embedded at the wall boundary elements. They concluded that such composite walls would fail in a flexural mode. With the additional steel tubes, the seismic performance of walls would become much better than RC walls. Among all the specimens, the wall with two steel tubes embedded at each boundary element showed superior performance in ductility, lateral load and also ultimate deformation due to the larger area ratio of steel tube. Ji et al. [16] studied the experimental seismic behaviour of steel tube-double steel plate-concrete composite walls. Experimental results revealed that with additional CFST boundary element, the seismic behaviour of the specimens increased significantly, as indicated by the larger deformation and energy dissipation capacity and slower degradation in rigidity and strength of the walls. Zhang et al. [17] proposed bundled lipped channel-concrete composite wall, in which cold-formed lipped channels were connected together by welding and served as the frame of the wall. They examined the seismic behaviour of the composite walls and figured out that by enhancing the boundary elements of the wall, the strength and stiffness degradation rate could be reduced and the deformation as well as the energy dissipation capacities could be increased. Ren et al. [18] investigated the seismic performance of four composite walls, i.e., traditional RC walls, walls with CFST, double-skin CFST and CFST-FRP confined concrete columns as boundary elements. Results showed that compared with conventional RC walls, the other three types of composite walls had excellent seismic resistance. Specimens with double-skin CFST and CFST-FRP confined concrete columns as boundary elements showed better performance than specimen with CFST column as boundary elements.

Most of the experimental tests of the RC or composite walls were stopped as the lateral load dropped to 85% of the peak lateral load after attaining the peak load. This may be attributed to the fact that the most of these walls would fail by compressive crushing of concrete at the bottom of the wall web. After yielding of wall web stirrups, the confinement effect to the concrete core would drop dramatically, causing severe concrete spalling. Thus, these walls could not withstand the large axial load acting at the top of the walls and failed. This situation can be even worse when adopting HSC. Moreover, as illustrated by Ren et al. [18], further research studies such as (1) enhancement of seismic resistance in the wall web and (2) more efficient connecting schemes between the boundary elements and wall web should be conducted. As a consequence, to effectively confine the wall web concrete and provide a better linkage between the wall web and boundary, a new form of confinement should be provided.

On the other hand, since the supplement of natural river sand (RS) gradually decreased in mainland China due to the environmental friendly requirement and sustainability of the country development, the price of RS became much more expensive. As a replacement, manufactured sand (MS), which is made by mechanical crushing of virgin rock, becomes more and more attractive in industry and research. Compared with RS, MS is different in shape, content of micro fines (rock deposits) and grading, resulting in different strength, workability and

durability properties of concrete [28–30]. To date, no research studies have been conducted on the behaviour of MS concrete composite walls. In tall building construction, the consumption of sand is huge and it is desirable to use MS as an alternative of RS. Therefore, it is necessary to study the seismic behaviour of walls with MS concrete.

In order to fill up the research gaps aforementioned, in this paper, an innovative composite wall with high-strength MS concrete, namely ring-stirrup CFST composite wall, is proposed. As suggested by Qian et al. [15], two CFST columns are embedded at each boundary element. Several stirrups in the form of continuous ring are provided along the entire section, detailed drawings will be provided in the following section. In the experimental tests, if there are n parameters and two variable levels per parameters, by using a traditional experimental design method, at least 2^n tests need to be conducted. For large or full scale experimental tests, it will become very costly and time-consuming using the traditional method. To study a relatively large number of parameters and variable levels with a small number of tests and at the same time maintain the accuracy of the experimental results, a systematic and efficient approach, namely, orthogonal experimental design method (Taguchi method), which was commonly adopted in the concrete mixing design or large scale experimental tests was introduced in this study [31–33]. By using the Taguchi method, at least 50% experimental tests could be waived, which is highly cost effective and time saving. The most important issue for Taguchi method is to choose the representative parameters. In this paper, three important parameters were selected: axial force ratio, steel ratio in CFST columns, which is defined as the ratio of steel tube area to the gross-sectional area of composite wall and the volume ring-stirrup ratio, which is defined as the ratio of ring-stirrup volume to the volume of ring-stirrup-confined core concrete. Each parameter contained two variable levels. Traditionally, a total of eight specimens should be prepared. By using the Taguchi method, only four walls were needed to be fabricated and tested under high axial force ratio and cyclic lateral load. The seismic performance of these four walls was evaluated in terms of the damage and failure modes, hysteresis loops of lateral force against top displacement, skeleton curves, strength and stiffness degradations as well as energy dissipation capacities. Test results revealed that the proposed form of composite wall showed superior seismic behaviour. Finally, a simplified design approach considering the confinement effect of CFST columns was proposed and verified to predict the lateral load-carrying capacity of the proposed walls.

2. Experimental program

2.1. Specimens

Specimens were designed to simulate the walls of lower floor in tall buildings. The Taguchi method using orthogonal arrays was adopted in the experiment. The following parameters were considered in the wall design: (1) axial force ratio; (2) steel ratio in CFST columns; (3) volume ring-stirrup ratio. The variation levels for the parameters were shown in Table 1a. According to the parameters and their variable levels in Table 1a, orthogonal array in the form of $L_4(2^3)$ can be obtained and details about the array can be seen in Table 1b. Therefore, a total of four composite walls were fabricated and tested under high axial force ratio and quasi-static cyclic lateral load. The walls are labelled CW1 to CW4 and the detailed information is provided in Fig. 1 and Table 1c. As it can be seen in Fig. 1a and b that the wall is 2000 mm in height and had a rectangular cross-section with 1000 mm (length) \times 200 mm (width). In order to fasten the walls and apply loading, foundation and top beams are casted and the sizes of them are 500 mm \times 500 mm and 250 mm \times 250 mm respectively. The lateral load is applied in the middle of top beam, resulting in an aspect ratio of 2.125 to ensure the flexure-dominated behaviour, which is similar to most of the research studies [15–18]. Two seamless steel tubes (Nominal yield stress 235 MPa, outer diameter 114 mm, thickness 3–4 mm) are embedded at

Table 1
Lists of specimens.

(a) Experimental parameters and the variation levels			
Parameters	Axial force ratio	Steel ratio in CFST columns	Ring-stirrup ratio
Variation level 1	0.5	2.09%	0.77%
Variation level 2	0.6	2.76%	0.96%
(b) Standard $L_4 (2^3)$ orthogonal array			
No. of tests	Axial force ratio	Steel tube thickness	Ring-stirrup ratio
1	1	1	1
2	1	2	2
3	2	2	1
4	2	1	2
(c) Lists of specimens			
No. of tests	Axial force ratio	Steel tube thickness (mm)	Ring-stirrup
1	0.5	3.0	Φ6@100
2	0.5	3.8	Φ6@80
3	0.6	3.8	Φ6@100
4	0.6	3.0	Φ6@80

each boundary element. The steel tubes are fully anchored within the foundation beam by welding at a 1000 mm × 200 mm × 5 mm steel cover plate, located below the transverse reinforcement of the foundation beam (Fig. 1h). CW1 and CW2 were tested under the upper limit of axial force ratio in the code, i.e., 0.5. In the meantime, CW3 and CW4 were designed to withstand a higher axial force ratio, which is beyond the limit stipulated in the code, i.e., 0.6. Detailed information of the axial force ratio calculation can be referred to the following section. For CW1 and CW4, the steel tube embedded was 3.0 mm thick while for the other two specimens, the thickness of the steel tube changed to 3.8 mm thick.

Fig. 1 also illustrates the reinforcing details. The reinforcement is designed as per seismic design code of buildings in China [7]. Φ10 steel bar (Nominal yield stress 400 MPa and diameter 10 mm) was selected as the longitudinal reinforcement along the cross-section. Conventionally, in rectangular-shaped cross section of RC walls, there is only 1 single closed stirrup with ties to form the stirrup skeleton. This type of transverse confinement cannot effectively confine concrete core since the confinement effect drops dramatically after steel yields. Without adequate confinement, cracks of concrete core would propagate quickly, causing failure of the specimens. In order to confine the wall web concrete more effectively and provide a better linkage between wall web and boundary, a new form of confinement using continuous steel ring along the entire section is proposed. It can be seen from Fig. 1c–e that along the cross section of the wall, a total of 6 stirrups with Φ6 steel bar (Nominal yield stress 500 MPa and diameter 6 mm) was provided. It can be seen in Fig. 1c–1e that the stirrups were bent into rectangular shape with 154 mm (width) × 170 mm (length) at both edges, 154 mm × 161 mm at the wall centroid and 154 mm × 186 mm in between, resulting in an overlapping of 16 mm per stirrup (Fig. 1c and d). Noted that for CW1 and CW3, the stirrups arranged at 100 mm centre-to-centre spacing (Fig. 1c), while for CW2 and CW4, the spacing was 80 mm along the elevation view of the specimens (Fig. 1d), resulting in the volume ring-stirrup ratio of 0.77% and 0.96% for CW1/3 and CW2/4 respectively. With this kind of stirrups, the walls can be divided into 6 zones. Each zone works

independently since each stirrup confines the concrete core inside. If one of the stirrup yields, the other 5 stirrups are still effective in confining the concrete core, resulting in slower degradation in strength and stiffness. Alternatively, all the zones can work together to resist strong earthquake since there is an overlapping of 16 mm between the stirrups. The energy induced by strong ground motion can be easily translated from one zone to the nearby zone. Thus, it is believed that this kind of confinement is excellent in resisting the seismic load. At the meantime, the reinforcement design for foundation and top beams can be referred to Fig. 1b and f–h, which fulfils the code requirement [7]. To have a better visualisation of the composite walls, the photograph of which before pouring concrete is shown in Fig. 1i.

2.2. Material properties

Three grades of concrete were adopted in the experiment. C40 ordinary commercial concrete was adopted to cast the foundation and top beams. C80 MS concrete was used for the concrete inside the steel tube while C60 MS concrete was used for the concrete outside the steel tube. Extensive studies showed that [28,29] MS concrete had higher strength but lower workability compared to RS concrete. Therefore, the mixing of MS sand concrete should be carefully designed. By replacing the cement partially with silica fume and/or powder material, using suitable superplasticizer, the flowability and cohesiveness of concrete could increase simultaneously [34–36]. The mixing of high-strength MS concrete is showed in Table 2. For the MS concrete, six standard cubes (150 mm × 150 mm × 150 mm) were casted and cured under the same condition of the walls. The MS concrete cubes were tested at 28 days. The cube compressive strength (f_{cu}), tensile strength (f_t), design strength (f_{cd}) and test strength (f_{ct}) as well as the elastic modulus (E_c) were recorded in Table 3. To attain material properties for longitudinal steel, stirrup and steel tube, three standard tensile coupons were tested as per Chinese standard [37] for each type of steel. The yield stress of reinforcement (f_{sy})/steel tube (f_{sy}), ultimate stress of reinforcement (f_{su})/steel tube (f_{su}) and elastic modulus of reinforcement (E_s) or steel tube (E_a) were recorded in Table 4.

2.3. Instrumentations and test set-up

In this experiment, the Hangzhou Bangwei pseudo-static testing equipment (Model: WAW-J12000J) in the structural lab of Shenzhen University was adopted. The maximum vertical load of the equipment is 12,000 kN, while the maximum horizontal push and pull loads are 2500 kN and 2000 kN, respectively. Detailed information of test set-up and instrumentations are shown in Figs. 2 and 3. The foundation beam was fixed to the reaction floor by four high-strength anchor bolts. The top beam was clamped to two hydraulic actuators (Vertical and horizontal). A steel plate was installed between the vertical hydraulic actuator and the top beam to evenly distribute the axial load to the wall. During loading process, the centres of vertical and horizontal hydraulic actuators could move freely to accommodate the deformation of walls. Vertical and horizontal loads are directly obtained by the equipment while the displacements and strains are measured by linear variable differential transducers (LVDTs) and strain gauges, respectively. Fig. 3 illustrated the locations of LVDTs and strain gauges. It can be seen from Fig. 3a that a total of five LVDTs (100 mm stroke) were installed horizontally to measure the lateral displacement of the walls. Among them, 3 LVDTs were mounted at 500 mm interval along the height of the wall. The other 2 LVDTs were mounted on the middle of foundation and top beams, respectively. From Fig. 3b–c it can be seen that 24 strain gauges were installed at the external face of one steel tube, which were located

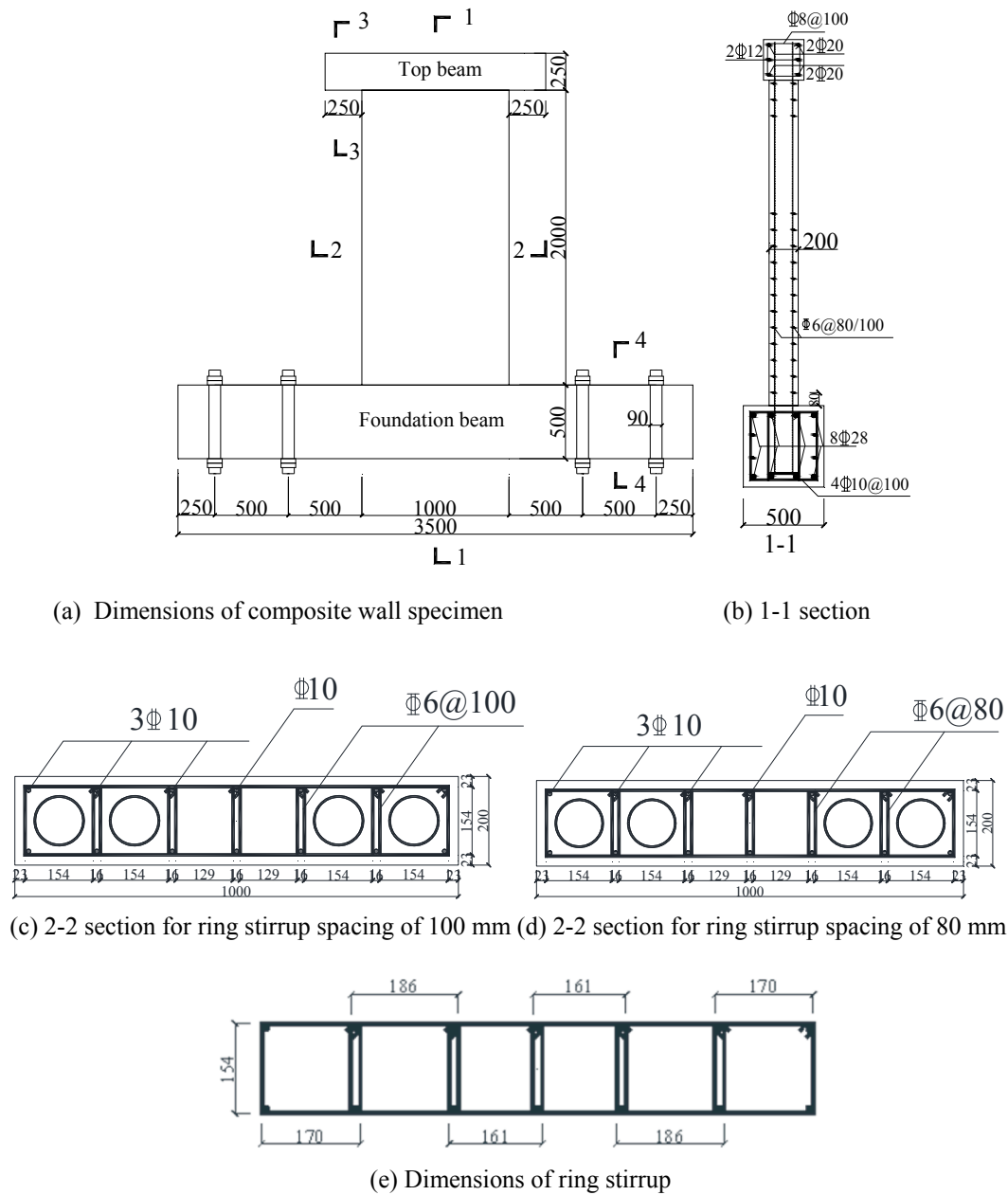


Fig. 1. Details of specimens.

at the base, 400 mm and 1000 mm above the base of the walls. At each layer, there were 4 pairs of strain gauges 90° separated from each other to measure the longitudinal and transverse strains. Other 78 strain gauges were installed on the surface of the longitudinal and transverse reinforcements (base, 400 mm and 1000 mm above the base of the walls) to monitor the strains developed at these locations. Each of the 174 strain gauges was marked with a unique ID for the following discussions, as shown in Fig. 3c–d.

2.4. Testing procedure

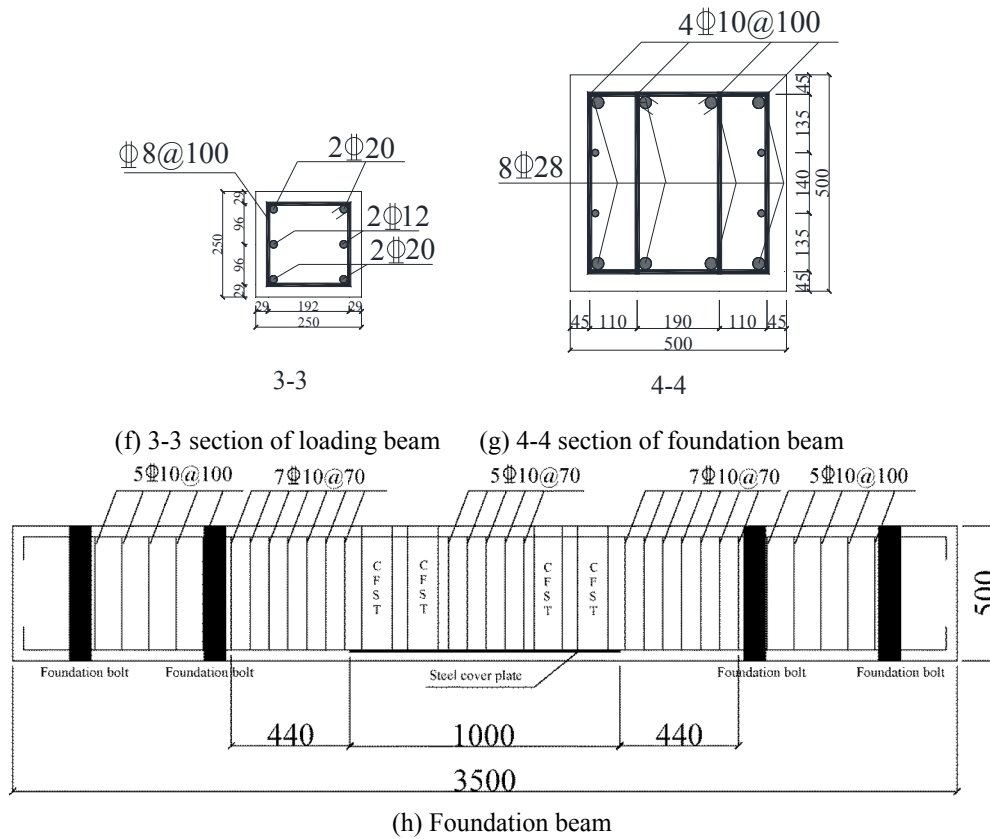
As described previously, the axial force ratio was one of the most important factors in the construction of the wall. With higher axial

force ratio, the depth of the compression zone of the wall would increase and as a result the deformation capacity as well as ductility of the wall decreased. Thus, the axial force ratio is considered to be the most important factor in the experimental design. In this study, the axial force ratio is derived from the following equations:

$$n_t = N_t / (f_{co,t} A_{co} + f_{ci,t} A_{ci} + f_{a,t} A_a) \tag{1}$$

$$n_d = N_d / (f_{co,d} A_{co} + f_{ci,d} A_{cc} + f_{a,d} A_a) \tag{2}$$

where n is the axial force ratio; N represents the constant axial force; f_{co} and f_{ci} are compressive strength of concrete outside and inside steel tube, respectively; f_a denotes the yield strength of steel tube; A_{co} and A_{ci} denote cross-section area of concrete outside and inside steel tube,



(i) Photograph of the composite wall before concrete casting

Fig. 1. (continued)

Table 2
Mixing of high-strength MS concrete.

	Cement kg	Water kg	Silica fume kg	Mineral powder kg	Sand kg	Big stone kg	Small stone kg	Water reducing (large) kg	Water reducing (small) kg
C80/m ³	455	143	65	130	710	798.75	266.25	12.48	3.12
C60/m ³	380	180	70	120	680	758.25	252.75	10.94	2.74

Water reducing (large) and water reducing (small) are two different types of water reducing in Sika Visconcrete series. The water reducing (small) in the table has antifoaming effect. Water reducing (large) and water reducing (small) are mixed with a mass ratio of 4:1.

Table 3
Material properties of high-strength MS concrete.

Concrete strength	Material properties of concrete				
	f_{cu} (MPa)	f_{cd} (MPa)	f_{ct} (MPa)	f_t (MPa)	E_c (GPa)
C60	60.1	27.6	38.6	3.8	35.3
C80	84.9	38.1	53.3	4.3	37.5

Table 4
Material properties of reinforcement and steel tube.

Steel type	Yield stress (MPa)	Ultimate stress (MPa)	Elastic modulus (GPa)
	f_{sy}/f_{ay}	f_{su}/f_{au}	E_s/E_a
Φ10 Steel bar	402	545	197
Φ6 Steel bar	498	619	187
Q235 (114μ ₁ 3.8)	323	416	180
Q235 (114μ ₁ 3.0)	336	432	181

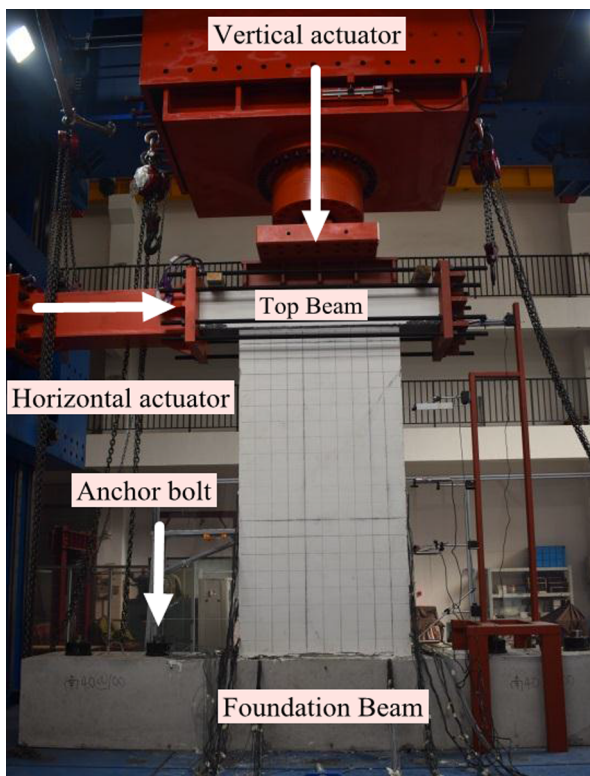


Fig. 2. Test set-up.

respectively; A_a denotes area of steel tube; the subscripts d and t mean respectively the design and test values. As per Chinese Code GB50011-2010 [7], $N_d = 1.2 N_c$. As shown in Table 3, the design and test strengths of C60 concrete are respectively 27.6 and 38.6 MPa, C80 are respectively 38.1 and 53.3 MPa.

Using Eqs. (1) and (2) with the design axial force ratios of 0.5 for CW1-2 and 0.6 for CW3-4, the constant axial loads applied on CW1-4 were respectively 2810, 2920, 3510 and 3380 kN. The experimental

axial force ratios are 0.29 for CW1-2 and 0.35 for CW3-4, which is presented in Table 5.

In order to ensure that the wall was in perfect contact with the vertical and horizontal loading platens and to eliminate the gaps inside the wall, before the experiment began, a small axial load in the magnitude of 20% of the constant axial force (Test value of axial force in Table 5) was applied, and then followed by a small lateral load. After preloading, the axial load was applied again and maintained at a constant value in the testing process (Test value of axial force in Table 5). After that, lateral load was applied at a quasi-static rate by a hybrid control method. As shown in Fig. 4, before wall yielded, it was tested under load control mode and one cycle was applied at each force level with loading rate equal to 60 kN/min. The peak load for the first cycle was 100 kN in both push and pull directions. The peak load for the latter cycle was increased at 100 kN increment for each cycle. After yielding of specimen, displacement control was adopted and three cycles were repeated at each displacement level. The loading rate was 6 mm/min. The displacement increased in the sequence of 0.5 times of yield displacement. In each cycle, a push load was applied then followed by a pull load. Unless otherwise specified, the push load was taken as positive and vice versa. The test was stopped as the lateral load dropped to 60% of the maximum lateral force or the specimen was severely damaged (Specimens lost its vertical load-carrying capacity) whichever was earlier.

3. Experimental results and discussions

The seismic performance of these four walls was evaluated in terms of the damage and failure modes, hysteresis loops of lateral force against top displacement, skeleton curves, strength and stiffness degradations as well as energy dissipation capacities in the following analysis.

3.1. Definition of yield, peak and ultimate points

For the convenience of discussions in the following sections, yield, peak and ultimate points are defined first based on the skeleton curve of CW1 in Fig. 5. (1) Peak point: the point where maximum lateral load is attained, as indicated by point “P” with coordinate (Δ_p, F_p) . (2) Yield point: defined by R-park method, which is schematically shown by point “Y” with coordinate (Δ_y, F_y) in Fig. 5. To be more specified, point “A” with axial load equal to $0.6F_p$ is figured out first, and then followed by a straight line OA intersecting the horizontal line BP (perpendicular to y-axis) at point “B”. Point “Y” is given as the intersection of line BY (perpendicular to x-axis) and the lateral load-top displacement curve. (3) Ultimate point: the ultimate displacement Δ_u is defined as the displacement when the lateral load has dropped to 60% of the peak load F_p after reaching the peak. Therefore, point “U₆₀” with coordinate (Δ_u, F_u) is defined as ultimate point, where $F_u = 60\% F_p$. As reported before, all the experimental tests in the literatures defined the ultimate state at which the lateral force is reduced to $0.85F_p$ after reaching F_p . Therefore, to make a meaningful comparison, point “U₈₅” with coordinate (Δ_{u85}, F_{u85}) , where $F_{u85} = 85\% F_p$, is shown in Fig. 5 and will also be used for the following section.

3.2. Damage and failure modes

The damage and failure modes of all the specimens at points Y, P, U₈₅ and U₆₀ are shown in Fig. 6. From the figure, it can be observed that:

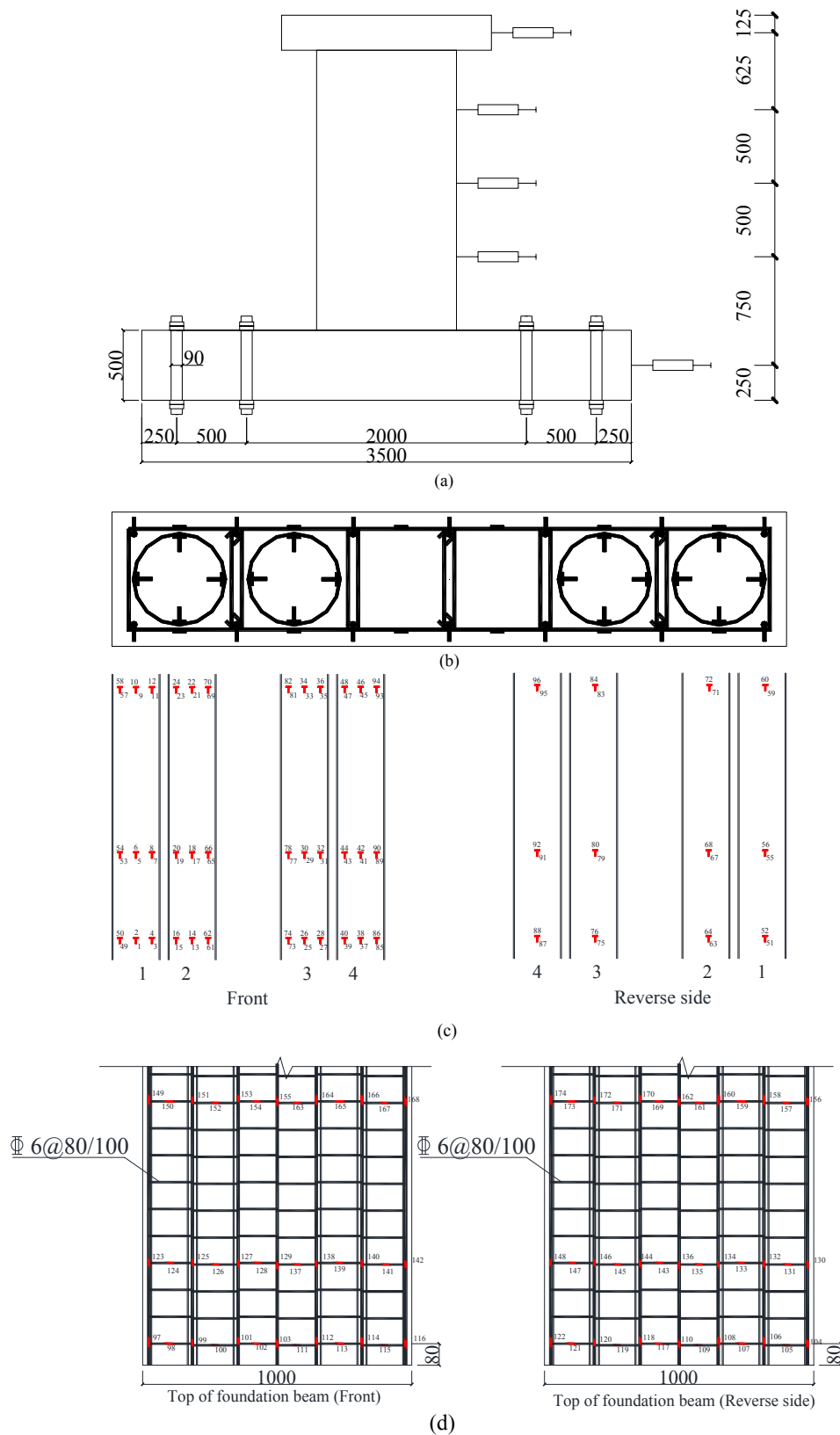


Fig. 3. Position of the sensors.

(1) Before yielding, all the specimens behaved elastically in this stage. Fig. 6a showed that cracks were not detected for CW1, CW3 and CW4. Micro-cracks inclined at 45° were observed for CW2 when the specimens yielded. For CW4, it can be seen that concrete cover was spalling slightly at the bottom of the wall.

(2) As the lateral load increased, cracks occurred and well developed for all the specimens, followed by the spalling of concrete cover, mainly at the bottom of the walls. Fig. 6b showed the status of specimens at which the lateral load reached peak stage. New cracks were developed inclined at 45° and the extending of existing cracks

Table 5
Design and experimental axial force ratio.

No. of tests	Test value of axial force (kN)	Axial force ratio	
		Design value	Test value
1	2810	0.5	0.30
2	2920	0.5	0.30
3	3510	0.6	0.36
4	3380	0.6	0.36

was seen. The cracks were firstly initiated at the bottom of the walls and distributed along the height of the wall due to the transfixion of the micro-cracks. It can be seen that the cracks were severer for CW1/2 than CW3/4, which may be attributed to the fact that the axial force ratio of the latter specimens was higher and it restricted the development of cracks at the initial stage.

- (3) It can be seen in Fig. 6c that when the lateral load dropped to 85% of the peak load, concrete cover continued to spall off, along with the exposure of stirrups in the proximity of wall base. At this stage, minor concrete crushing at the corner of wall base can be seen. Therefore, strength and stiffness were degraded slightly. Unlike other walls reported by literatures previously with significant reduction in the walls' axial load-carrying capacity when the lateral load dropped to 85% of the peak load, the axial load-carrying capacity remained unchanged for the ring-stirrup CFST composite walls proposed in this study, which demonstrated that the confinement in the form of ring-stirrup was very effective.
- (4) At the ultimate stage, it can be seen in Fig. 6d that at the locations of concrete cover spalling, ring-stirrups were yielded and some of the longitudinal steel bars were buckled. At the bottom corner of the two edge embedded columns, it can be seen that the concrete crushed more seriously than U_{85} . However, only inclined cracks were observed for the middle wall web without concrete crushing at the bottom. It should be noticed that at this stage, the axial load applied kept the constant value though the lateral load dropped to 60% of the peak load. This again verified that due to the composite

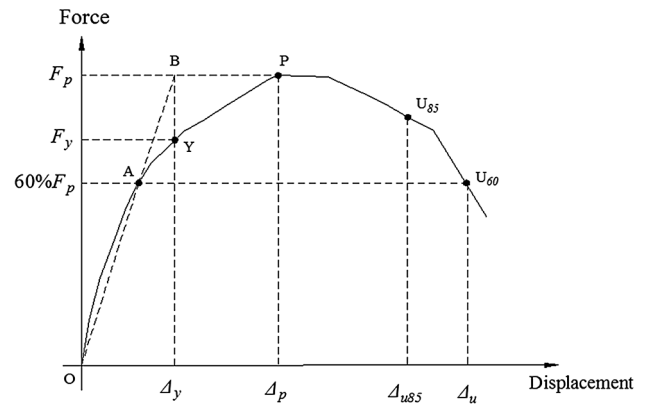


Fig. 5. Definition of yield, peak and ultimate points.

action of CFST columns and the effective confinement of ring-stirrups, the proposed ring-stirrup CFST composite wall was highly effective in preventing the collapse of the wall under very high axial force ratio.

It should be noticed that the concrete cover spalling in the wall web can be improved by enclosing the ring-stirrups by a large stirrup, which should be one of the tasks in the further study.

3.3. Lateral forces against top displacement relationships

The measured lateral force against top displacement hysteresis curves for all the walls were shown in Fig. 7, while the key points introduced previously, i.e., point Y, P, U_{85} and U_{60} were marked on the curves. Generally speaking, it can be observed from Fig. 7 that all the loops were fat and behaved like parallelograms without any pinching effect, which demonstrated the flexural behaviour. To be more detailed, at the initial load-controlled loading stage, i.e., from point O to point Y, the lateral load increased linearly and rapidly. Under loading and unloading at this stage, the hysteresis loops behaved linear-elastically

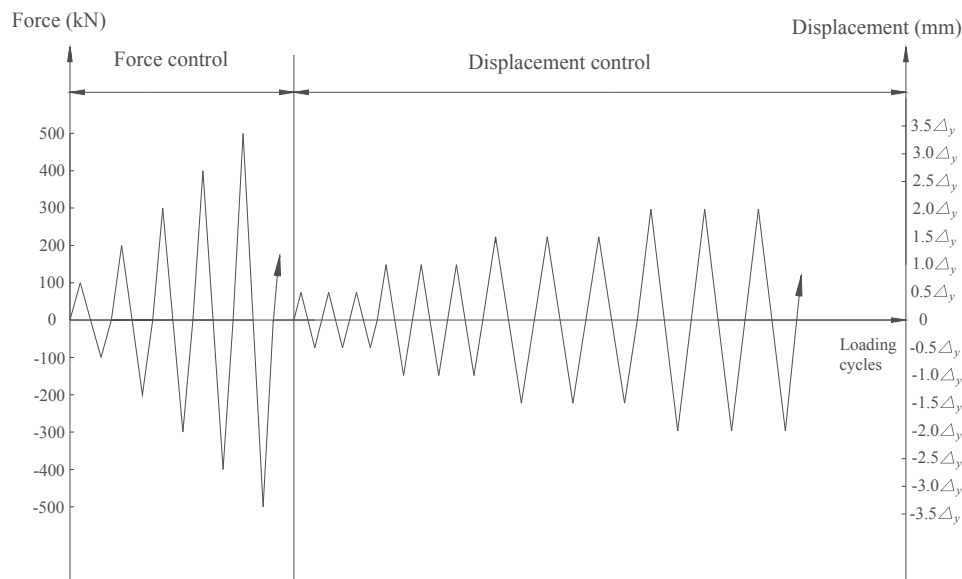


Fig. 4. Loading history of lateral load.

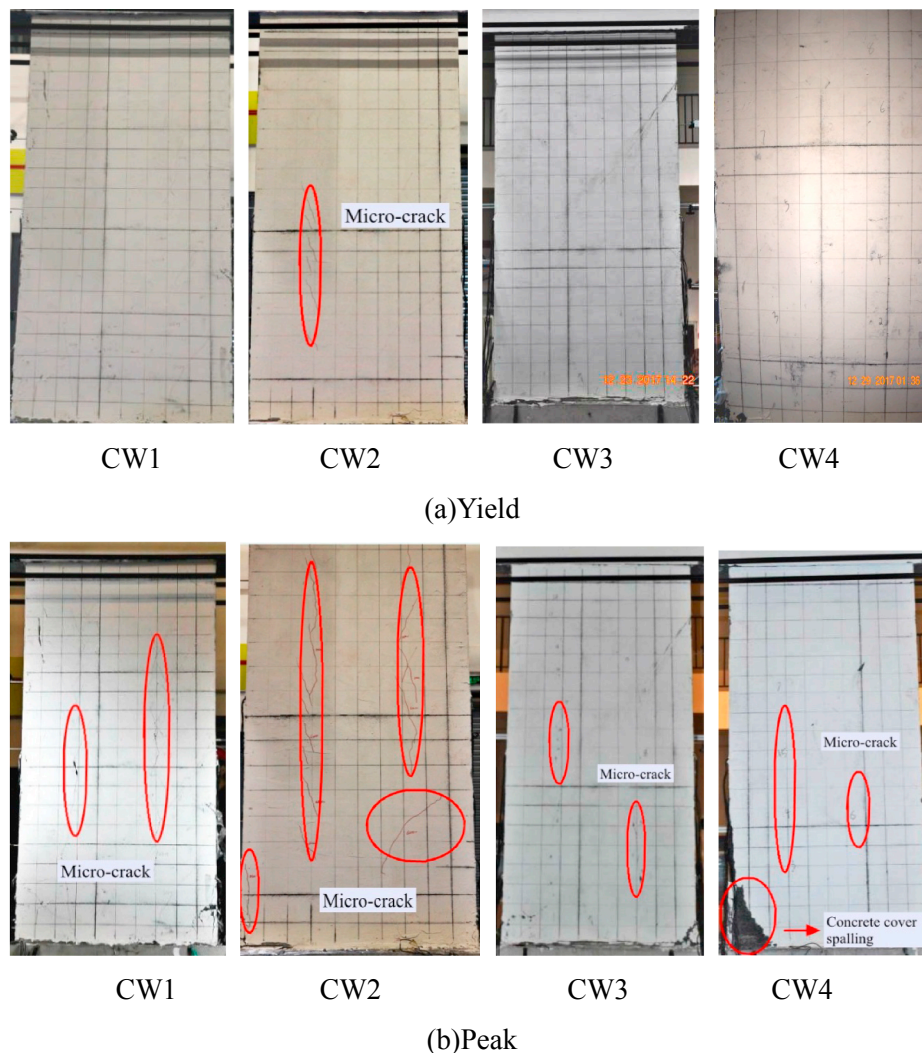


Fig. 6. Damage and failure modes for all the specimens.

without any residual displacement. From point Y to point P, the curves increased much more slowly, indicating the degradation in stiffness. Moreover, residual displacement was observed in this stage, showing non-linearly plastic characteristic. From point P to point U_{85} , the strength dropped steadily and slowly with larger residual displacement at unloading, which indicated very good ductility performance of the walls. At point U_{85} , it is noticed that the residual displacements for CW1-4 were respectively 11.35, 8.63, 5.82, and 6.33 mm, with corresponding residual drift ratios (θ) after unloading of 0.534%, 0.406%, 0.274% and 0.298%, where $\theta = \Delta/H$, and H is the height from the bottom of the wall to the middle of the top plate and is equal to 2125 mm in this study. Compared with specimen CFST-W (axial force ratio of 0.5, C40 wall web concrete and C20 CFST concrete) in [18] (residual displacement 37.21 mm and $\theta = 1.96\%$) and specimen CW2-CW3 (axial force ratios from 0.55 to 0.60, C40 wall web concrete and C50 CFST concrete) in [15] (residual displacement from 15.43 to 23.67 mm and θ from 0.566% to 0.869%), it can be concluded that though with higher strength MS concrete in-filled, which was reported by researchers that this type of concrete was much more brittle than normal concrete [38,39], residual displacements at U_{85} of the proposed composite walls in this study were the smallest, showing better performance in deformation recovery and more ductile behaviour. It again proved that the proposed confining scheme of the composite wall was highly effective in improving the ductility and thus the earthquake

resistance of the walls. From point U_{85} to U_{60} , the area enclosed by the loops increased rapidly with the increment in residual displacement.

3.4. Skeleton curves

The envelope curves of the lateral force against top displacement were plotted in Fig. 8. The F_y , F_p , F_{u85} and F_u were recorded in Table 6. The displacements Δ_y , Δ_p , Δ_{u85} and Δ_u as well as the corresponding drift ratios θ_y , θ_p , θ_{u85} and θ_u were reported in Table 7. In Tables 6 and 7, it should be noted that the values were the average values of loads and displacements measured in the push and pull directions due to the symmetry nature of the skeleton curves. Before yielding, all the walls shared the same slope, indicating the small differences in initial stiffness (around 120 – 130 kN/mm) of the specimens. The lateral load kept increasing with smaller stiffness to the peak level. After the peak point, the lateral load-carrying capacity started to decrease with modest rate, indicating very ductile performance. From Table 7 and Fig. 8, it can be seen that Δ_{u85} for CW1-CW4 were respectively 39.71, 37.15, 25.96, and 29.94 mm. Comparing with the residual displacements previously (11.35, 8.63, 5.82, and 6.33 mm), it could be figured out that the deformations were recovered by 28.36, 28.52, 20.14, and 23.61 mm. Noted that specimen C FST-W (axial force ratio of 0.5, C40 wall web concrete and C20 CFST concrete) in [18], the deformations were recovered by 26.10 mm (residual displacement 37.21 mm and

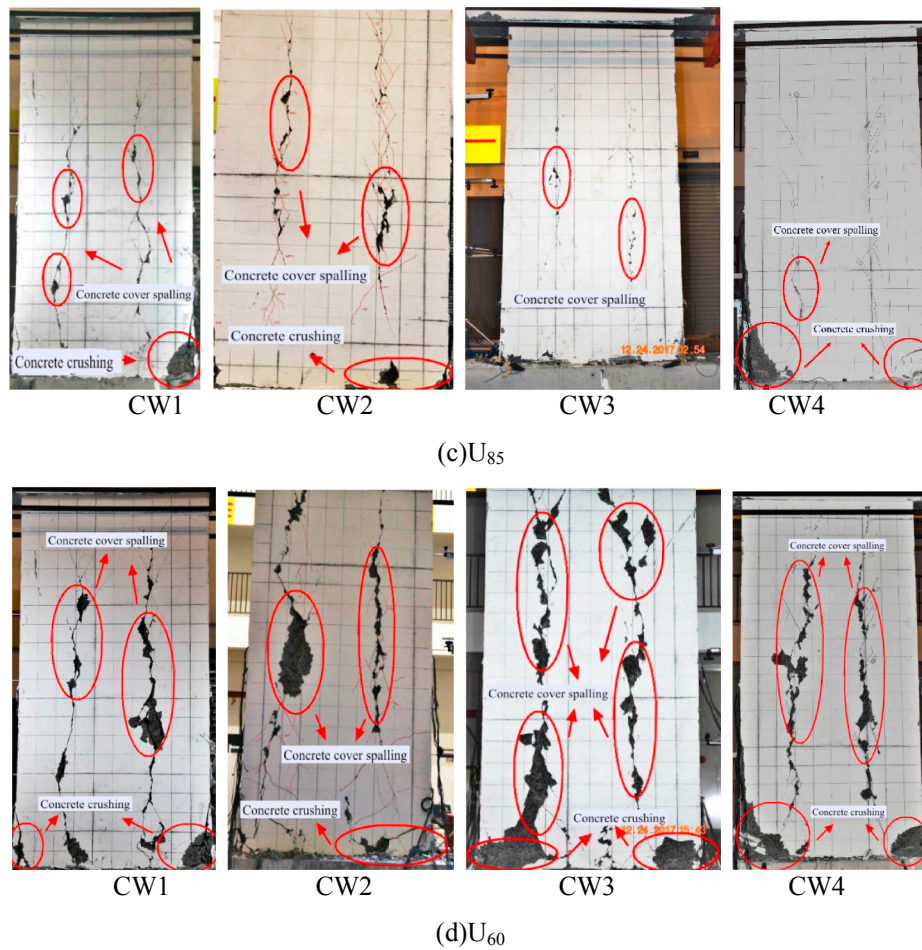


Fig. 6. (continued)

$\theta = 1.96\%$) and specimen CW2-CW3 (axial force ratios from 0.55 to 0.60, C40 wall web concrete and C50 CFST concrete) in [15], the deformations were recovered by 38.22 mm and 28.40 mm (residual displacement from 15.43 to 23.67 mm and θ from 0.566% to 0.869%), the composite walls in this study showed similar deformation recovery but much smaller residual displacement, indicating the superior performance in deformation recovery. The drift ratios at point U_{85} , $\theta_{U_{85}}$ were respectively 1.869%, 1.748%, 1.222%, and 1.409%, while at point U_{60} , θ_u were respectively 2.134%, 2.040%, 1.575%, and 1.707% for walls CW1-4, which were much larger than the limited drift ratio (1%) of structures at rarely occurred earthquakes [40]. However, under such extreme circumstance, the axial load-carrying resistance remained unchanged and there was no significant destabilizing problem of the walls, which fulfilled the requirement of “No collapse in strong earthquake”. This again proved excellent performances of the proposed walls subjected to severe earthquake loads, even under very high axial force ratio.

Since the Taguchi method was employed in the experimental design, the effects of axial force ratio, steel ratio of CFST columns and volume ring-stirrup ratio on the seismic behaviour of composite walls might not be clear enough. Therefore, range analysis method was adopted to figure out the functions of the three parameters separately. The flow chart of range analysis is shown in Fig. 9. As it can be seen in Fig. 9, the first step of range analysis is to calculate the value of K_{ij} , which is defined as summation of the experimental results (loads, displacements, drift ratio or ductility) corresponding to the i th variable and j th parameter (or i th level and j th factor). The second step is to get the value of k_{ij} , which is the average value of K_{ij} . According to the

principle of Taguchi method, since all the experiments were conducted in the same condition, if the effect of the 1st factor, say axial force ratio on the experimental result was very small, then the value of k_{11} and k_{21} should be similar and vice versa. After determining k_{ij} , the optimum level and combination of the levels could be obtained. The trend line showing the effects of different levels on the typical results could also be obtained. The third step is to determine the value of R_j and $R_j = \max(k_{ij}) - \min(k_{ij})$. The larger the value of R_j , the more important of the j th factor is.

The range analysis for F_p was shown in Table 8 and Fig. 10a. It can be noticed that with thicker steel tube, the peak strength increased. This is because as the steel tube thickness increased, the confining stress provided increased, which improved the strength of the confined concrete. This drew the same conclusions with the CFST columns [41–43]. Moreover, with smaller axial force ratio, the peak strength increased, which drew the same conclusions with composite walls in the literature. For example, CW3 and CW4 in Ref. [15], with axial force ratios of 0.60 and 0.72, the peak lateral loads were 738 and 771 kN; In Qiao et al. [44] experimental study, for specimens S3N1 and S3H1 with axial forces ratios of 0.15 and 0.25, the lateral load for S3H1 is 1.03 times of S3N1; Specimens WSL-1, WSL-4 and WSL-5 in Ref. [45] also illustrated the same phenomenon. This may be due to the fact that with smaller axial force ratio, the neutral axis decreased and the moment induced by the web concrete and CFST columns decreased and thus the peak lateral strength decreased. It is difficult to figure the effect of volume ring-stirrup ratio on F_p . As volume ring-stirrup ratio increased, the confining stress on web concrete became larger and more uniform, which would increase the strength of web concreted. However, this would decrease

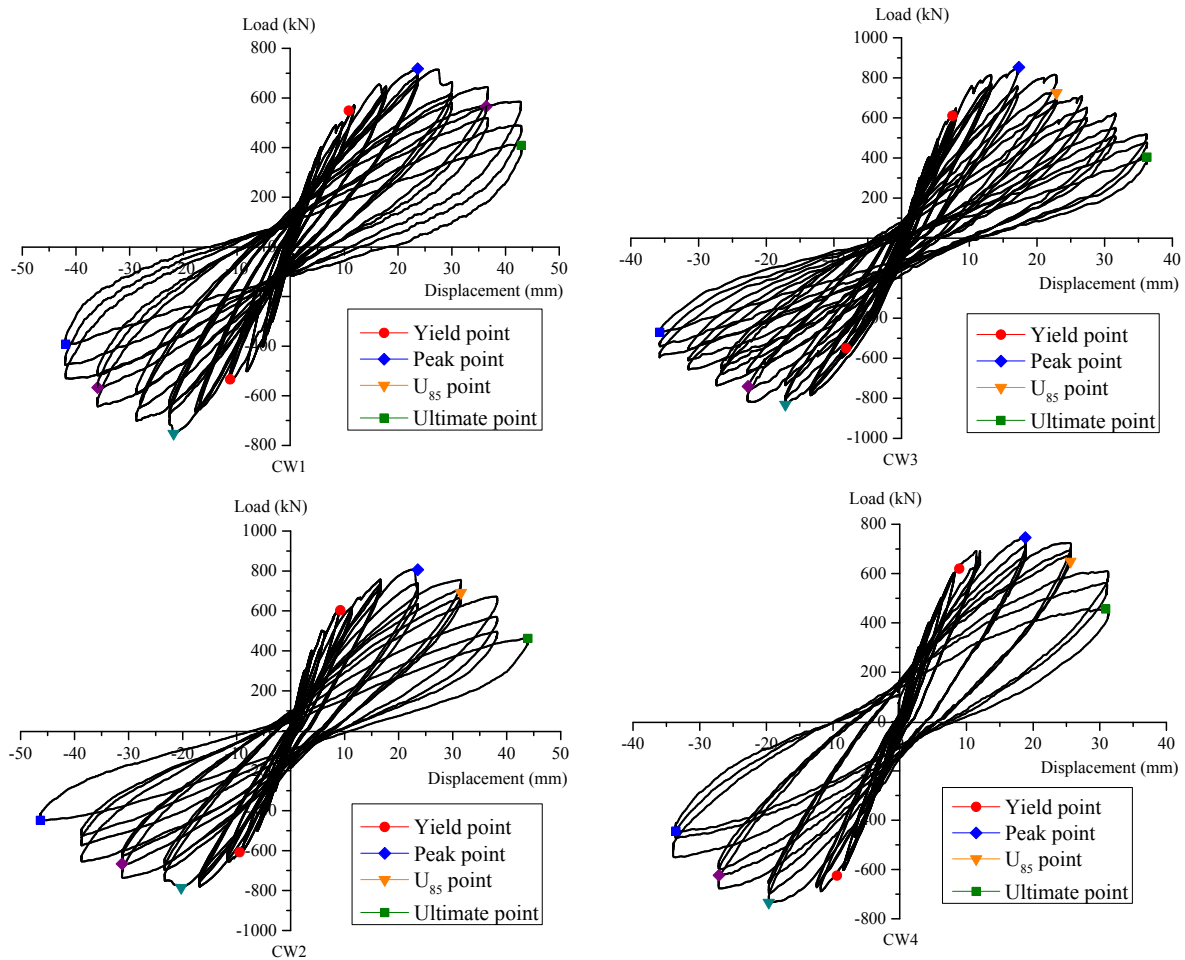


Fig. 7. Hysteresis loops of lateral forces against top displacement relationships.

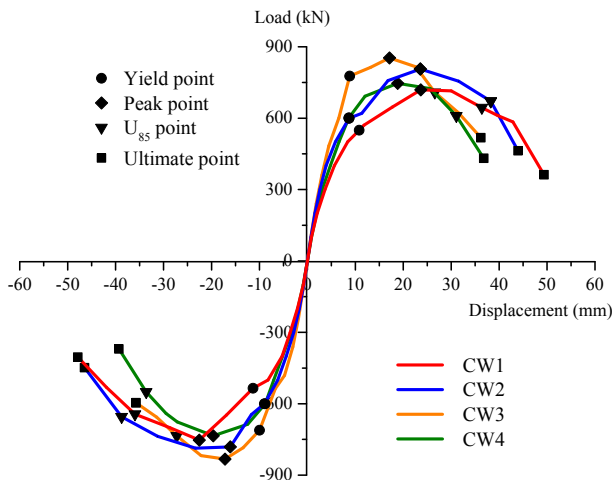


Fig. 8. Envelope curves of lateral forces against top displacement.

Table 6
Lateral load-carrying capacity of all the specimens.

No. of tests	F_y	F_p	F_{u85}	F_u	V_p	V_p/F_p
1	542.2	735.9	625.5	441.5	690.4	0.94
2	605.9	796.5	677	477.4	750.9	0.94
3	581.1	843.0	703.3	496.1	838.9	1.00
4	623.3	740.5	629.3	444.2	777.7	1.05

the neutral axis depth since the axial force ratio remained unchanged, which decreased the moment induced by the CFST columns and web concrete. Therefore, theoretical studies of effect of volume ring-stirrups ratio on the moment induced by the composite wall should be conducted.

In order to compare the ductility of all the specimens quantitatively, two ductility coefficients related to two specified limits of strength degradation, i.e., points U_{85} and U_{60} were defined:

$$\mu_{u85} = \frac{\Delta_{u85}}{\Delta_y} \tag{3}$$

$$\mu_u = \frac{\Delta_u}{\Delta_y} \tag{4}$$

where μ denotes the ductility coefficient.

All the ductility values for CW1-4 were calculated in Table 7. In this table, it can be observed that the range of μ_{u85} was from 3.35 to 4.02, which satisfied the demand of the code with ductility ≥ 3.0 [40]. The range of μ_u was from 4.06 to 4.69, which illustrated the confinement provided by steel tube in CFST embedded columns and ring-stirrups in the wall web can effectively improve the ductility of the specimens. The range analysis for ductility is shown in Table 8 and Fig. 10b and c. From the table and figures, it can be seen that the larger the axial force ratio, the smaller the μ_{u85} or μ_u was. This is obvious since the increase of axial force ratio would certainly decrease the ductility of structures. Thus, there are limitations of axial force ratio of 0.5 in various design codes to ensure a typical ductility level. As the steel ratio of CFST columns or volume ring-stirrups ratio became larger, the ductility increased. This is because increasing the steel tube thickness or the decreasing the

Table 7
Key displacements and ductility of all the specimens.

No. of tests	Δ_y	Δ_p	Δ_{u85}	Δ_u	μ_1	μ_1	μ_1	μ_1	μ_{u85}	μ_u
1	10.81	23.65	39.71	45.34	0.509%	1.113%	1.869%	2.134%	3.67	4.19
2	9.24	23.55	37.15	43.36	0.435%	1.108%	1.748%	2.040%	4.02	4.69
3	7.52	17.13	25.96	33.47	0.354%	0.806%	1.222%	1.575%	3.45	4.44
4	8.94	18.83	29.94	36.27	0.421%	0.886%	1.409%	1.707%	3.35	4.06

spacing of ring-stirrup could improve the confinement effect, and thus enhance the ductility. Apparently, the steel ratio of CFST columns played a more important role in the ductility behaviour of specimens than volume ring-stirrup ratio. The reason is that though the amount of confined-concrete was smaller, the CFST embedded columns could provide larger flexural resistance due to the larger level arm. Another possible reason may be due to the fact that the ductility of CFST columns is much larger than the ring-stirrup confined concrete wall web [46].

In order to observe the overall lateral deformation of the composite wall, the readings of LVDTs located horizontally at 500 mm, 1000 mm, 1500 mm and 2125 mm away from the base of the wall were recorded along the height of the wall at the point of Y, P, U₈₅ and U₆₀ in Fig. 11. The figure revealed that generally speaking, the lateral displacement increased as the height of the wall increased. Before peak stage, the lateral displacements were distributed approximately linearly along the height of the wall. At the ultimate stage, the lateral displacements of the upper wall increased more rapidly than the lower part, showing that the wall was dominated by flexural deformation.

3.5. Stiffness and strength degradation

In this paper, the secant stiffness is adopted for the stiffness analysis, which is defined as:

$$K_i^+ = \frac{|P_i^+|}{|\Delta_i^+|} \tag{5}$$

$$K_i^- = \frac{|P_i^-|}{|\Delta_i^-|} \tag{6}$$

where K_i^+ and K_i^- denote the positive and negative secant stiffness at the i th loading cycle, respectively; P_i^+ and P_i^- are respectively the push and pull peak loads at the i th loading cycle; Δ_i^+ and Δ_i^- denote the displacement corresponding to P_i^+ and P_i^- at the i th loading cycle, respectively.

The secant stiffness was plotted against the lateral top displacement for all the composite walls in Fig. 12. It is evident from the figure that initially, the stiffness was basically identical for all the specimens, showing that the material properties of all the walls agreed well with each other. Besides, all the specimens shared similar stiffness degradation with the increasing lateral displacement. The curves dropped rapidly at the beginning but much more slowly at the later stage. This is because the development of initial micro-cracks of concrete degraded the stiffness seriously. However, after the damage of the concrete, the lateral loads were transferred to the embedded CFST columns, which was much steadier in mechanical properties than ring-stirrup confined concrete wall web.

To further assess the strength degradation behaviour of the specimens, the strength degradation factor η is defined as follows:

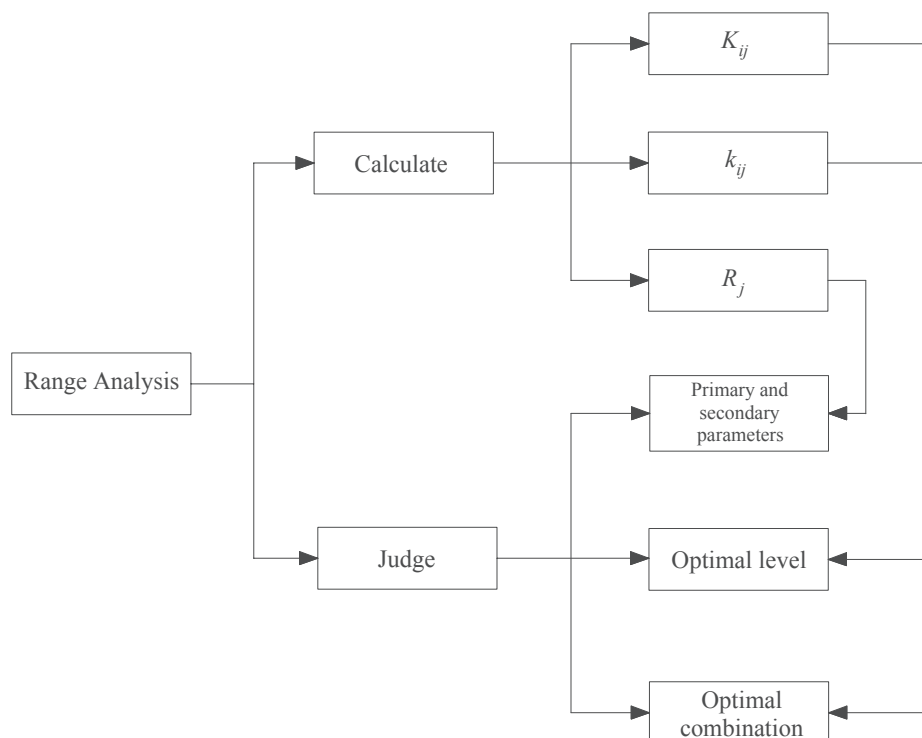


Fig. 9. Flow chart of range analysis.

Table 8
Range analysis for the experimental results.

No. of tests	Parameters (Factors)			
	A (Axial force ratio)	B (steel ratio of CFST columns)	C (Ring-stirrup ratio)	
1	1 (0.5)	1 (2.09%)	1 (0.77%)	
2	1	2 (2.76%)	2 (0.96%)	
3	2 (0.6)	2	1	
4	2	1	2	
F_p	K_1	1532.4	1476.40	1578.9
	K_2	1583.50	1639.5	1537.00
	k_1	766.2	738.2	789.5
	k_2	791.8	819.8	768.5
	R	25.6	81.6	21.0
	Order of factors	B > A > C		
	Optimum level Optimum combination	A2 A2B2C1	B2	C1
μ_{u85}	K_1	7.69	7.02	7.13
	K_2	6.80	7.47	7.37
	k_1	3.85	3.51	3.56
	k_2	3.40	3.74	3.68
	R	0.45	0.23	0.12
	Order of factors	A > B > C		
	Optimum level Optimum combination	A1 A1B2C2	B2	C2
μ_u	K_1	8.89	8.25	8.64
	K_2	8.50	9.13	8.75
	k_1	4.44	4.13	4.32
	k_2	4.25	4.57	4.37
	R	0.19	0.44	0.06
	Order of factors	B > A > C		
	Optimum level Optimum combination	A1 A1B2C2	B2	C2
E_c	K_1	271.94	247.18	247.71
	K_2	234.77	259.53	259.00
	k_1	135.97	123.59	123.86
	k_2	117.39	129.77	129.50
	R	18.59	6.17	5.65
	Order of factors	A > B > C		
	Optimum level Optimum combination	A1 A1B2C2	B2	C2

$$\eta = \frac{P_j^3}{P_j^1} \tag{7}$$

where P_j^3 and P_j^1 denote the maximum strength of the 3rd and 1st cycle at the same lateral displacement (Δ_j), respectively;

No strength degradation before yielding since only one loading cycle was performed at each load level at the load control stage. The strength degradation coefficient curves were shown in Fig. 13. It can be observed that the trend of η was similar for all the four specimens and it decreased as the lateral displacement increased. Before attaining the peak lateral load, η was quite stable and decreased slowly. However, after the peak point, η began to drop more dramatically and the minimum value of η was about 0.7 at ultimate state of the wall.

3.6. Energy dissipation capacity

As it is known to all, the energy dissipation capacity is one of the most important factors in seismic design. The dissipated energy in each loading cycle E is equal to the area enclosed by the corresponding hysteresis loop of lateral force against top displacement as per Fig. 7 and the cumulative energy E_t is equal to the summation of E . The E and E_t against lateral displacement are shown in Fig. 14. It can be noticed in the figure that the E and E_t increased as the top displacement or lateral

load increased. Moreover, it can be seen in Fig. 14a that at each displacement level after yielding of specimens, the dissipated energy in the latter cycle was always smaller than the one in the former cycle, which is due to the degradation of strength in each loading cycle, as illustrated in Section 3.5. From Fig. 14b, it can be observed that E_t at ultimate state were 130.1, 141.9, 117.6 and 117.1 kNm for specimens CW1-4, respectively. From range analysis in Table 8 and Fig. 10d, it can be figured out that as the axial force ratio decreased or the steel ratio of CFST columns/volume ring-stirrup ratio increased, the energy dissipation capacity increased. This is because with smaller axial force ratio or larger steel ratio of CFST columns/volume ring-stirrup ratio, the strength and ductility of specimens were enhanced and thus the energy dissipation capacity. Among the three parameters, the axial force ratio exhibited greatest impact on the energy dissipation capacity.

4. Proposed model for lateral load-carrying capacity evaluation

As it has been mentioned previously, a total of 174 strain gauges were used to monitor the strain developed on different locations of the walls, which can be seen in Fig. 3. The strains at typical loading stages (Yield, Peak and U_{85}) and critical locations were given in Table 9. It could be seen in Table 9 the axial strains on the outer steel tube at the base of the wall (strain gauge no. 49 in Fig. 3) were -1214, -5734 and -10870 for CW1 at points Y, P and U_{85} , respectively, which were always much larger than the axial strains in magnitude on the opposite steel tube (strain gauge no. 85 in Fig. 3) due to the large axial force applied. The axial strains on the longitudinal reinforcement at the edge of the wall base (strain gauge no. 97 in Fig. 3) were -2100, -5734, -11951, which were larger than the readings of strain gauge no. 49 in magnitude since the location of strain gauge no. 97 was further away from the neutral axis than no. 49. Comparing the strains at the base and 400 mm from the base of the wall, it can be seen in Table 9 that obviously the strains at the base were larger in magnitude. Thus, it is believed that the base of the walls would always be the most critical part.

The strains at the steel tube and longitudinal reinforcement at the base of the walls were plotted against the length of the wall at points Y, P, U_{85} and U_{60} in Fig. 15. It can be observed that before point P, the axial strains were distributed approximately linearly, implying that the wall could keep its integrity and there was no out-of-plane bending, which means the plane section remained plane assumption was appropriate until peak lateral strength was attained. From point U_{85} to U_{60} , the axial strains of the edge wall increased more rapidly than the middle part. As the result, the plane section assumption was no longer valid.

It is evident that the behaviour of composite walls was dominated by flexural deformation and the wall base section was the most critical part of the walls. Therefore, it is believed that the lateral peak load could be evaluated based on the flexural strength of the wall base. Assumptions were made as follows: (1) Assumption on the section: Plane section remained plane before peak lateral strength was achieved. This assumption was justified; (2) Assumptions on concrete: the confinement effect of core concrete inside CFST columns should be taken into account [42,46–48]. From the former analysis, the ring-stirrup was effective in confining the core concrete inside and providing better linkage between the boundary and wall web. Therefore, to consider the confining stress provided by ring-stirrup, confined concrete strength by should be used. Meanwhile, the unconfined concrete strength should be adopted at concrete covers. The equivalent rectangular stress block theory was adopted to calculate the compressive strength of concrete other than the one inside CFST columns, in which average stress αf_c and the extent of x from the extreme compression fibre were assumed (x is the neutral axis depth, α is the strength parameter, for C60 concrete, $\alpha = 0.98$). Tensile strength of concrete was neglected; (3) Assumptions on steel tube: All the steel tubes yielded in compression and tension at peak stage. Evidently in Table 9, all the steel tubes at peak stage were in

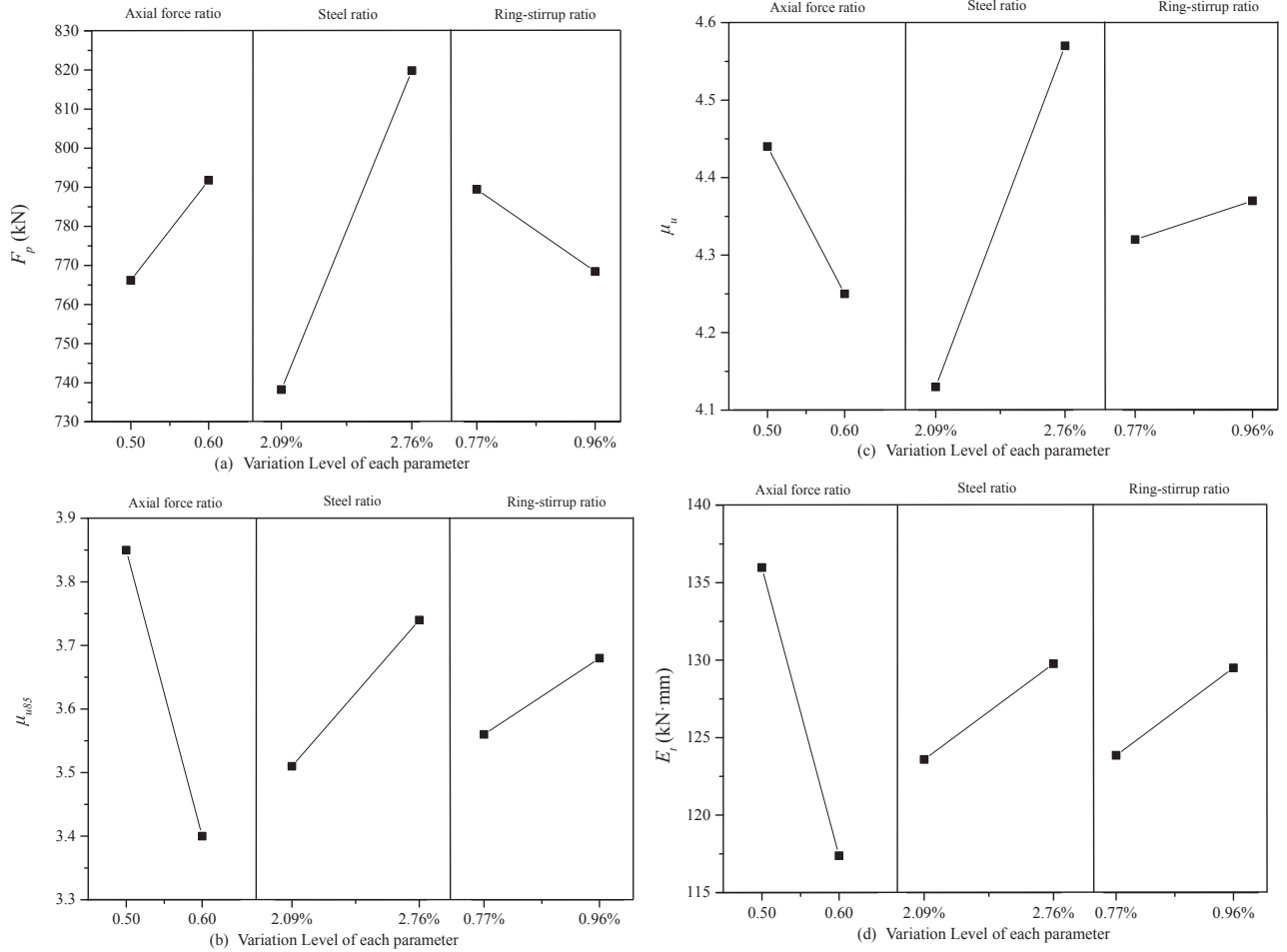


Fig. 10. Range analysis for experimental results.

yielding plateau. Therefore, yield strength of steel tube was adopted to assess the lateral peak load of the composite walls; (4) Assumptions on reinforcements: The longitudinal reinforcements in the wall web were closed to the neutral axis and strain gauge readings showed that the strains developed there were quite small (Average less than 1/15 yield strain, the largest one closed to 1/3 yield strain). Therefore, the contribution of them were ignored and only the 8 longitudinal reinforcements at the boundary elements were assumed to be yielded, in which 4 reinforcements were in tension and others were in compression.

Based on the force and moment equilibrium with respect to the centroid of the wall, from the free-body-diagram in Fig. 16, the following equations can be obtained:

$$N = N_c + 2N_{CFST-C} - 2N_{CFST-T} \quad (8)$$

$$M_p = 0.5N_c(h_w - x) + A_s f_{sy}(h_w - 2a_s) + 2N_{CFST-C}(0.5h_w - a_a) + 2N_{CFST-T}(0.5h_w - a_a) \quad (9)$$

$$N_c = \alpha f_{ccw} \left((b_w - 2b_c)x - \frac{\pi}{2} D^2 \right) + \alpha f_{cw} (b_w b_c + 2b_c x) \quad (10)$$

$$N_{CFST-T} = A_a f_{ay} \quad (11)$$

$$M_p = HV_p + N \Delta_p \quad (12)$$

where N , N_c , N_{CFST-C} , N_{CFST-T} denote the axial load applied, concrete compressive strength outside CFST columns, axial compressive and tensile loads of CFST columns; M_p is the flexural strength at the wall bottom section under N ; h_w is the wall depth; x is the neutral axis depth;

A_s , f_{sy} are the area and yield stress of the longitudinal reinforcement, respectively; a_s and a_a are the distances of the longitudinal reinforcement centroid and steel tube centroid to the nearest wall edge, respectively; b_w and b_c are the wall width and concrete cover width, respectively; D is the outer diameter of steel tube; A_a and f_{ay} are the area and yield stress of steel tube, respectively; H is the height of the lateral loading point to the base of the wall, which is equal to 2125 mm in this study; V_p is the predicted lateral load-carrying capacity.

The confined concrete strength of wall web f_{ccw} can be calculated using the following equation as suggested by Furlong [49].

$$f_{ccw} = f_{cw} \left(1 + 4.1 \frac{f_{rt}}{f_{cw}} \right) \quad (13)$$

in which f_{cw} is the unconfined concrete cylinder strength of wall web; f_{rt} is the confining stress provided by the ring-stirrup.

Thanks to the composite action between steel tube and core concrete, the ultimate strength of CFST columns could be significantly enhanced. Therefore, the following design approach [50,51] was adopted to calculate the compressive strength of CFST columns at peak stage of the walls. This approach was verified by comparing 286 experimental tests and 782 parametric study results and very good agreement was obtained. Detailed information of the approach was listed below.

Firstly, an empirical equation was given to relate the tensile hoop stress $\sigma_{s\theta}$ of steel tube to the uni-axial yield strength of steel tube f_{ay} at peak stage of CFST columns:

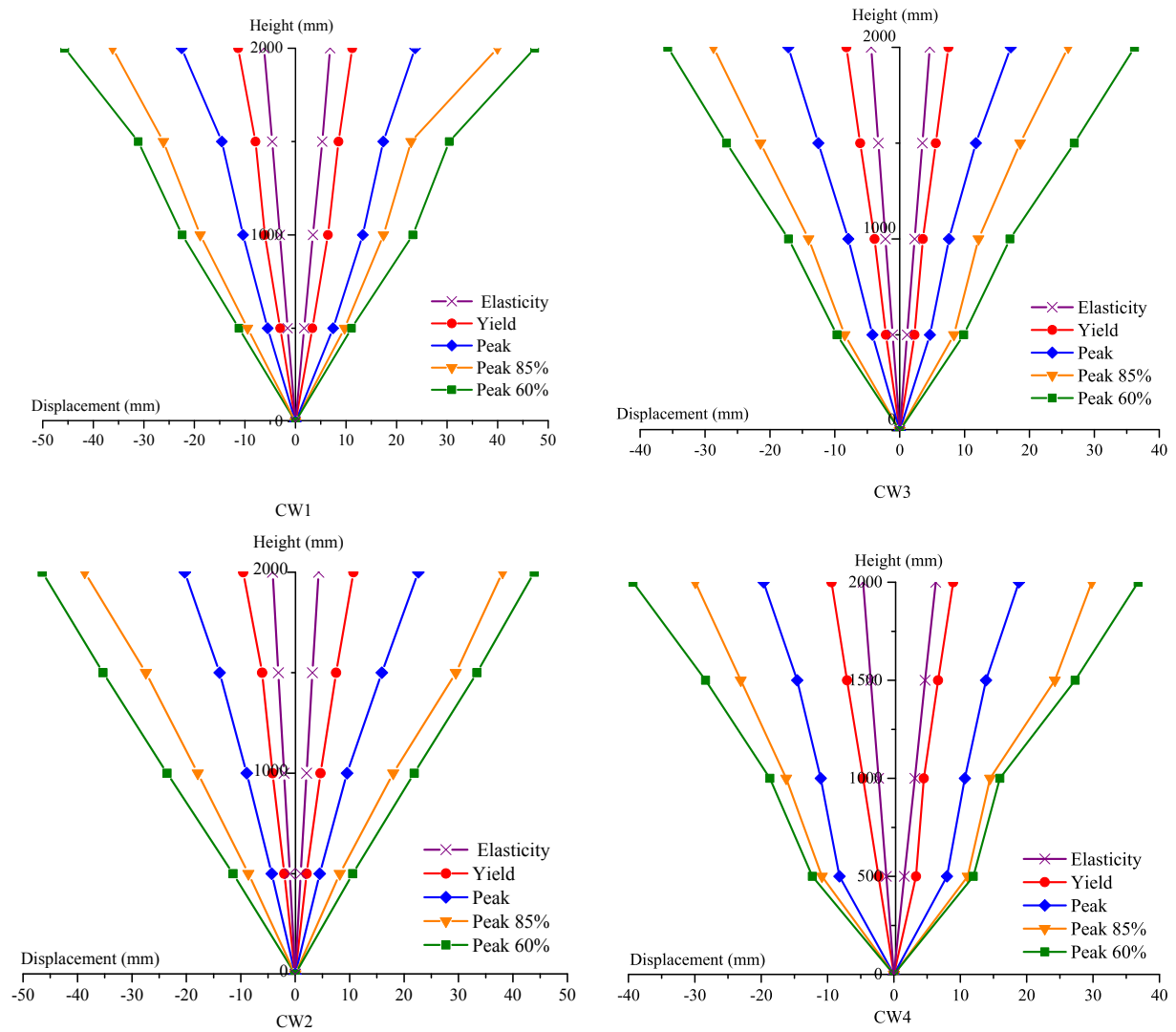


Fig. 11. Lateral displacement profiles along the walls.

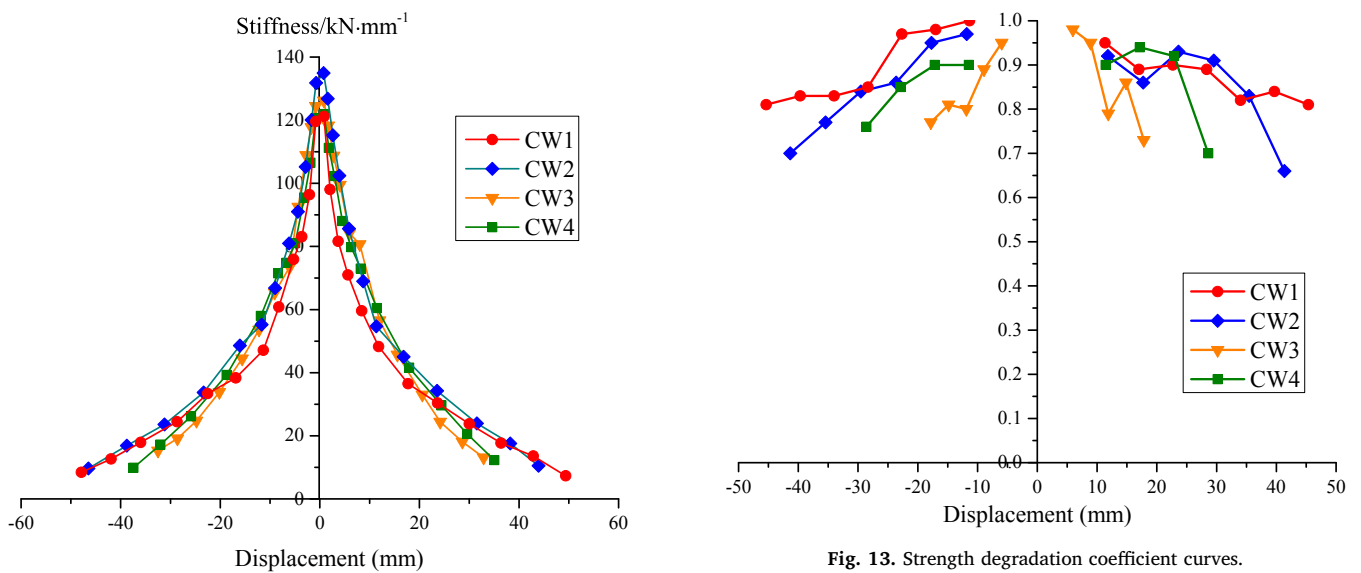


Fig. 12. Secant stiffness degradation curves.

Fig. 13. Strength degradation coefficient curves.

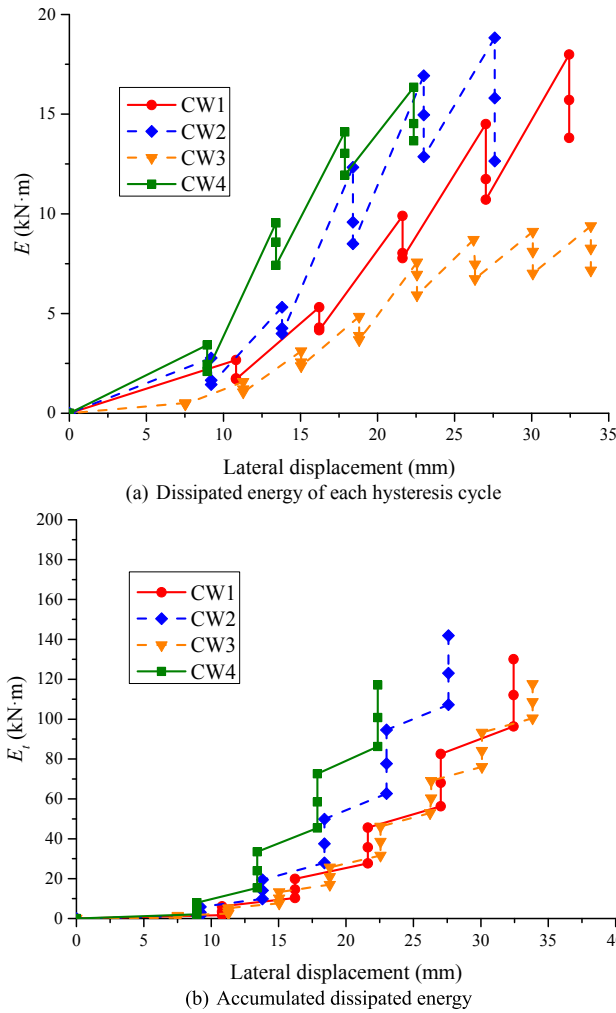


Fig. 14. Energy dissipation curves for specimens.

$$\frac{\sigma_{s\theta}}{f_{ay}} = -0.2 \left(\frac{D}{t} \right)^{0.35} \left(\frac{f'_c}{f_{ay}} \right)^{0.45} \quad (14)$$

Secondly, for thin-walled steel tube, the radial stress of steel tube could be ignored, resulting in bi-axial stress state of steel tube. According to Von Mises yield criterion, the following equation could be established:

$$\sigma_{s\theta}^2 - \sigma_{s\theta}\sigma_{sz} + \sigma_{sz}^2 = f_{ay}^2 \quad (15)$$

Thirdly, the confined concrete stress at peak strength of CFST columns, f_{ccp}^* could be evaluated by:

$$\frac{f_{ccp}^*}{f'_c} = 1 + 3.5 \left(\frac{f_r}{f'_c} \right) \quad (16)$$

$$f_r = - \frac{2t}{D - 2t} \sigma_{s\theta} \quad (17)$$

where f'_c is the unconfined concrete cylinder strength inside steel tube and f_r is the confining stress.

Lastly, the peak compressive strength of CFST columns, N_{CFST-C} could be calculated by summing up the strength of steel tube and concrete, respectively.

$$N_{CFST-C} = \sigma_{sz}A_a + f_{ccp}^*A_c \quad (18)$$

where A_c respectively the cross-sectional areas for steel tube and concrete. For CFST columns at peak stage, the A_a and A_c could be assumed as unchanged since the axial deformation was quite small.

The concrete strength adopted in the model (f_{cw} or f'_c) is the cylinder strength, the converting equation from concrete cube strength to cylinder strength is listed below [46]:

$$f_{cyl} = 0.8513f_{cu} - 1.5998 \quad (19)$$

f_{cyl} and f_{cu} are respectively the concrete cylinder and cube strengths;

The predicted lateral load-carrying capacity was compared with the experimental lateral strength in Table 6. Very good agreements have been obtained with the predicted-to-experimental ratios range from 0.94 to 1.05 (on average 0.98) and very small deviation of 0.0525.

Table 9
Strain of shear walls at typical loading stages and critical locations.

Strains of CW1 ($\mu\epsilon$)								
Location	Base of wall				400 mm from the base of the wall			
	Steel tube		Longitudinal reinforcement		Steel tube		Longitudinal reinforcement	
Strain Gauge	49	85	97	116	53	89	123	142
Point Y	-1214	743	-2100	1145	-598	671	-1379	771
Point P	-5734	1382	-5734	1845	-1304	1751	-2195	1167
Point U_{85}	-10870	3711	-11951	3602	-10565	2602	-8351	6944
Strains of CW2 ($\mu\epsilon$)								
Strain Gauge	49	85	97	116	53	89	123	142
Point Y	-1429	970	-1387	1029	-598	640	-745	794
Point P	-7750	1220	-1789	2890	-1314	954	-2485	1657
Point U_{85}	-10800	4427	-3500	5600	-2810	14,177	-44324	17,037
Strains of CW3 ($\mu\epsilon$)								
Strain Gauge	49	85	97	116	53	89	123	142
Point Y	-1328	2200	-2324	1923	-780	640	-358	794
Point P	-2615	12,513	-2753	4770	-2314	1905	-1243	1183
Point U_{85}	-5914	12,513	-3023	5831	-5672	2195	-44324	17,037
Strains of CW4 ($\mu\epsilon$)								
Strain Gauge	49	85	97	116	53	89	123	142
Point Y	-1344	907	-1978	828	-787	949	-1978	828
Point P	-1489	889	-2258	1302	-2761	3147	-2258	1302
Point U_{85}	-1789	1218	-2903	2430	-2830	1190	-2903	2430

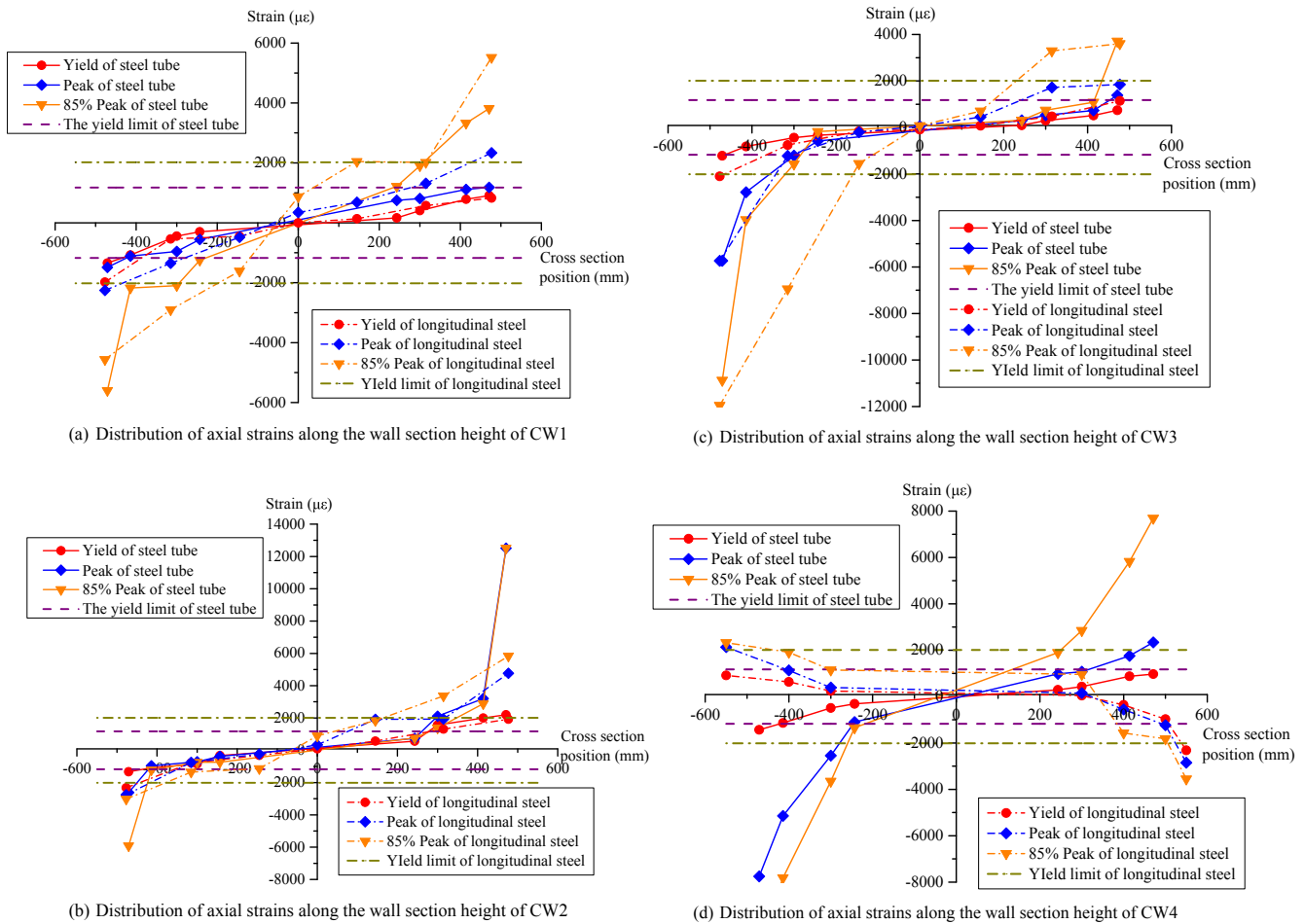


Fig. 15. Distribution of axial strains along the wall section height.

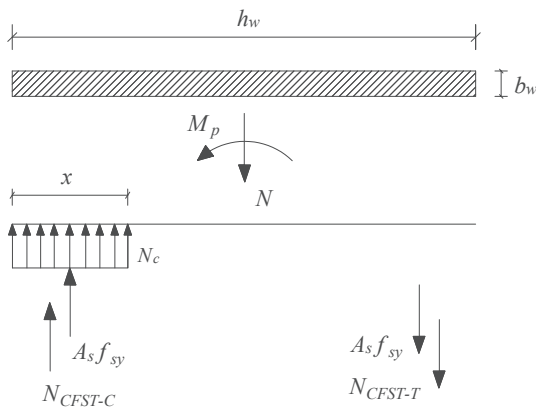


Fig. 16. Free-body-diagram of wall section.

5. Conclusions

In this study, an innovative composite wall, namely ring-stirrup CFST composite wall with high-strength MS concrete was proposed. A series of experimental tests based on orthogonal experimental design method (Taguchi method) were conducted to study the seismic behaviour of the composite walls. The experimental parameters were axial force ratio, steel ratio in CFST columns and volume ring-stirrup ratio. From the test results, the following conclusions could be made:

(1) For all the composite walls, the axial load applied kept the constant value though the lateral load dropped to 60% of the peak load,

indicating that the embedded CFST columns and the ring-stirrup were effective in preventing the collapse of the walls even under very high axial force ratio.

- (2) Evidently, the proposed composite walls were dominated by flexural deformation, since the concrete showed compressive crush at the wall base, the longitudinal reinforcements and the steel tube at wall boundary yielded and the lateral displacements of the upper wall increased more rapidly than the lower part.
- (3) The hysteresis loops of lateral forces against top displacement were fat and parallelograms without any significant pinching effect, which demonstrated the flexural behaviour of walls.
- (4) The proposed confining schemes of the composite walls were highly effective in improving the ductility and thus the deformability.
- (5) Due to the development of initial micro-cracks of concrete, the stiffness degradation was larger at the beginning but much more slowly at the later stage. Before attaining the peak lateral load, the strength degraded slowly. However, after the peak point, the strength degradation factor η began to drop more dramatically and the minimum value of η was about 0.7 at ultimate state of the wall.
- (6) With thicker steel tube or smaller axial force ratio, the peak strength increased. The effect of volume ring-stirrup ratio is quite complicated and should be studied theoretically.
- (7) As the axial force ratio decreased or the steel ratio of CFST columns/volume ring-stirrup ratio increased, the ductility and energy dissipation capacity of walls increased.

Finally, by validating the plane section remained plane assumption before peak stage, a design approach considering the enhancement effect of wall web concrete due to the ring-stirrup and the confinement

effect of CFST columns was proposed to calculate the lateral load-carrying capacity of the proposed walls. By comparing the predicted and experimental results, it is concluded that very good agreements have been obtained and the validity of the proposed design approach has been verified.

Acknowledgements

The authors acknowledge the support of this research from the Intellectual Innovation Program of Shenzhen Science and Technology Innovation Committee, China (Grant No: JCYJ20170818142117164 and JCYJ20160331114415945), and from the Natural Science Foundation of Shenzhen University, China (Grant No: 2017062). The funding supported by Foshan Kern Intelligent Electric Appliance Co. Ltd. is gratefully acknowledged (Grant No: 59047).

References

- [1] Lefas ID, Kotsosovos MD, Ambraseys NN. Behavior of reinforced concrete structural walls. Strength, deformation characteristics, and failure mechanism. *ACI Struct J* 1990;87(1):23–31.
- [2] Su RKL, Wong SM. Seismic behaviour of slender reinforced concrete shear walls under high axial load ratio. *Eng Struct* 2007;29(8):1957–65.
- [3] Thomsen JH, Wallace JW. Displacement-based design of slender reinforced concrete structural walls – experimental verification. *J Struct Eng* 2004;130(4):618–30.
- [4] Li LZ, Liu X, Yu JT, Lu ZD, Su MN, Liao JH, et al. Experimental study on seismic performance of post-fire reinforced concrete frames. *Eng Struct* 2019;179(1):161–73.
- [5] EN 1998-1. Eurocode 8: Design of Structures for Earthquake Resistance—Part 1: General Rules, Seismic Action and Rules for Buildings. Brussels: European Committee for Standardization, CEN; 2004.
- [6] ACI 318-08. Building Code Requirements for Structural Concrete and Commentary. Farmington Hills: American Concrete Institute; 2008.
- [7] GB 50011-2010. Code for Seismic Design of Buildings. Beijing: China Ministry of Construction; 2010. [In Chinese].
- [8] Mander JB, Priestley MJN, Park R. Theoretical stress-strain model for confined concrete. *J Struct Eng*, ASCE 1988;114(8):1804–26.
- [9] Ho JCM, Lam JYK, Kwan AKH. Effectiveness of adding confinement for ductility improvement of high-strength concrete columns. *Eng Struct* 2010;32(3):714–25.
- [10] Ho JCM, Pam HJ. Inelastic design of low-axially loaded high-strength reinforced concrete columns. *Eng Struct* 2003;25(8):1083–96.
- [11] Wang L, Su RKL, Cheng B, Li LZ, Wan L, Shan ZW. Seismic behavior of preloaded rectangular RC columns strengthened with precambered steel plates under high axial load ratios. *Eng Struct* 2017;152:683–97.
- [12] Wang L, Su RKL. Strengthening of preloaded RC columns by post compressed plates—a review. *Struct Eng Mech* 2018;65(4):477–90.
- [13] Ho JCM, Lam JYK, Kwan AKH. Flexural ductility and deformability of concrete beams incorporating high-performance materials. *Struct Des Tall Special Build* 2012;21(2):114–32.
- [14] Zhou J, Wang L. Repair of fire-damaged reinforced concrete members with axial load: a review. *Sustainability* 2019;11(4):963.
- [15] Qian J, Jiang Z, Ji X. Behavior of steel tube-reinforced concrete composite walls subjected to high axial force and cyclic loading. *Eng Struct* 2012;36:173–84.
- [16] Ji X, Jiang F, Qian J. Seismic behavior of steel tube–double steel plate–concrete composite walls: experimental tests. *J Constr Steel Res* 2013;86:17–30.
- [17] Zhang X, Qin Y, Chen Z. Experimental seismic behavior of innovative composite shear walls. *J Constr Steel Res* 2016;116:218–32.
- [18] Ren F, Chen J, Chen G, Guo Y, Jiang T. Seismic behavior of composite shear walls incorporating concrete-filled steel and FRP tubes as boundary elements. *Eng Struct* 2018;168:405–19.
- [19] Mohamed N, Farghaly AS, Benmokrane B, Neale KW. Numerical simulation of mid-rise concrete shear walls reinforced with GFRP bars subjected to lateral displacement reversals. *Eng Struct* 2014;73:62–71.
- [20] Petkune N, Donchev T, Hadavinia H, Wertheim D, Limbachiya M. Comparison of the behaviour of steel, pure FRP and hybrid shear walls under cyclic seismic loading in aspect of stiffness degradation and energy absorption. *Constr Build Mater* 2018;165:621–30.
- [21] Chen MT, Young B. Material properties and structural behavior of cold-formed steel elliptical hollow section stub columns. *Thin-Walled Struct* 2019;134:111–26.
- [22] Chen MT, Young B. Cross-sectional behavior of cold-formed steel semi-oval hollow sections. *Eng Struct* 2018;177:318–30.
- [23] Lai MH, Ho JCM. Axial strengthening of thin-walled concrete-filled-steel-tube columns by circular steel jackets. *Thin-Walled Struct* 2015;97:11–21.
- [24] Lai MH, Ho JCM. Effect of continuous spirals on uni-axial strength and ductility of CFST columns. *J Constr Steel Res* 2015;104:235–49.
- [25] Teng JG, Huang YL, Lam L, Ye LP. Theoretical Model for Fiber-Reinforced Polymer-Confined Concrete. *J Compos Constr* 2007;11(2):201–10.
- [26] Lai MH, Ho JCM. Optimal design of external rings for confined CFST columns. *Mag Concr Res* 2015;67(19):1017–32.
- [27] Lai MH, Ho JCM. Behaviour of uni-axially loaded concrete-filled-steel-tube columns confined by external rings. *Struct Des Tall Special Build* 2014;23(6):403–26.
- [28] Shen W, Yang Z, Cao L, Cao L, Liu Y, Yang H, et al. Characterization of manufactured sand: Particle shape, surface texture and behavior in concrete. *Constr Build Mater* 2016;114:595–601.
- [29] Jaya Prithika A, Sekar SK. Mechanical and fracture characteristics of Eco-friendly concrete produced using coconut shell, ground granulated blast furnace slag and manufactured sand. *Const Build Mater* 2016;103:1–7.
- [30] Zhao S, Ding X, Zhao M, Li C, Pei S. Experimental study on tensile strength development of concrete with manufactured sand. *Constr Build Mater* 2017;138:247–53.
- [31] Li D, Song X, Gong C, Pan Z. Research on cementitious behavior and mechanism of pozzolanic cement with coal gangue. *Cem Concr Res* 2006;36(9):1752–9.
- [32] Lin Y-H, Tyan Y-Y, Chang T-P, Chang C-Y. An assessment of optimal mixture for concrete made with recycled concrete aggregates. *Cem Concr Res* 2004;34(8):1373–80.
- [33] Ozbay E, Oztas A, Baykasoglu A, Ozbebek H. Investigating mix proportions of high strength self compacting concrete by using Taguchi method. *Constr Build Mater* 2009;23(2):694–702.
- [34] Lai MH, Hanzic L, Ho JCM. Fillers to improve passing ability of concrete. *Struct Concrete* 2019;20(1):185–97.
- [35] Maybury J, Ho JCM, Binhowimal SAM. Fillers to lessen shear thickening of cement powder paste. *Constr Build Mater* 2017;142:268–79.
- [36] Binhowimal SAM, Hanzic L, Ho JCM. Filler to improve concurrent flowability and segregation performance of concrete. *Aust J Struct Eng* 2017;18(2):73–85.
- [37] GB/T 228.1-2010. Metallic materials Tensile testing [In Chinese]. Beijing: China Ministry of Construction; 2010.
- [38] Pilegis M, Gardner D, Lark R. An investigation into the use of manufactured sand as a 100% replacement for fine aggregate in concrete. *Materials* 2016;9(6):440.
- [39] Ding X, Li C, Xu Y, Li F, Zhao S. Experimental study on long-term compressive strength of concrete with manufactured sand. *Constr Build Mater* 2016;108:67–73.
- [40] Zhu M, Liu J, Wang Q, Feng X. Experimental research on square steel tubular columns filled with steel-reinforced self-consolidating high-strength concrete under axial load. *Eng Struct* 2010;32(8):2278–86.
- [41] Lai MH, Ho JCM. Confining and hoop stresses in ring-confined thin-walled concrete-filled steel tube columns. *Mag Concr Res* 2016;68(18):916–35.
- [42] Lai MH, Ho JCM. Experimental and theoretical studies of confined HSCFST columns under uni-axial compression. *Earthquakes Struct* 2014;7(4):527–52.
- [43] Ho JCM, Lai MH, Luo L. Uniaxial behaviour of confined high-strength concrete-filled-steel-tube columns. *Proc Inst Civil Eng – Struct Build* 2014;167(9):520–33.
- [44] Qiao QY, Cao WL, Li XY, Dong HY, Zhang WW, Yin F. Seismic behavior of shear walls with boundary CFST columns and embedded multiple steel plates: experimental investigation. *Eng Struct* 2018;160:243–56.
- [45] Wu L, Tian Y, Su Y, Chen H. Seismic performance of precast composite shear walls reinforced by concrete-filled steel tubes. *Eng Struct* 2018;162:72–83.
- [46] Lai MH, Ho JCM. A theoretical axial stress-strain model for circular concrete-filled-steel-tube columns. *Eng Struct* 2016;125:124–43.
- [47] Lai MH, Ho JCM. Confinement effect of ring-confined concrete-filled-steel-tube columns under uni-axial load. *Eng Struct* 2014;67:123–41.
- [48] Ho JCM, Lai MH. Behaviour of uni-axially loaded CFST columns confined by tie bars. *J Constr Steel Res* 2013;83:37–50.
- [49] Furlong RW. Strength of steel encased concrete beam-columns. *J Struct Div, ASCE* 1967;93(5):113–24.
- [50] Lai MH, Ho JCM. An analysis-based model for axially loaded circular CFST columns. *Thin-Walled Struct* 2017;119:770–81.
- [51] Lai MH, Chen MT, Ren FM, Ho JCM. Uni-axial behaviour of externally confined UHSCFST columns. *Thin-Walled Struct* 2019. <https://doi.org/10.1016/j.tws.2019.04.047>.